Numerical Analysis of Photonic Crystal Fibres.

Mariusz Rafał Zdanowicz, MSc.

Thesis submitted to the University of Nottingham
for the degree of Master of Research

February 2008

Abstract

Numerical methods for the simulation of photonic structures bring serious advantages in the field of research and design. Well prepared modelling techniques allow simulation of the demanded characteristics prior to fabrication of the device, or in some case the experimentally observed properties of fabricated devices to be understood in detail. .

This thesis describes work to develop a numerical algorithm based on the real distance paraxial finite-difference vectorial beam propagation method (FD-VBPM). The algorithm is based on Maxwell Equations, simplified to the time independent diffusion equation. The program was developed at the National Institute of Telecommunications in Warsaw. This work will describe the validation process of the code, and the problems encountered when the presented method was applied to the simulation of Photonic Crystal Fibres (PCF).

Acknowledgements

I would like to convey my gratitude to all who helped me to finish this dissertation. Particularly, I am obliged to Prof. Trevor Benson and Prof. Marian Marciniak for their kind help and great patience, and Dr Ella Becker for all the answers for my questions.

The List of Contents:

1. Introduction to Photonic Crystals and Photonic Crystal Fibres (PCF)

1.1. The genesis and development of photonic crystals.

Photonic Crystals are dielectric structures with a periodic distribution of the refractive index. The simplest form of a photonic crystal has one-dimensional periodic structure, for example multilayer film – a Bragg mirror. Electromagnetic wave propagation in such systems was first studied by Lord Rayleigh in 1887 [1]. This structure was the first photonic band gap structure created by man. However, the Photonic Band Gap (PBG) phenomena was described over one hundred years later [2]. The Bragg reflection was the basis for creating more complicated structures, 2D and 3D photonic crystals. Figure 1.1.1 introduces the basic classification of photonic crystals. The periodicity is in the material (typically dielectric) structure of the crystal. Only a 3D periodicity, with a more complex topology than is shown in figure 1.1.1 c), can support an omnidirectional photonic bandgap.

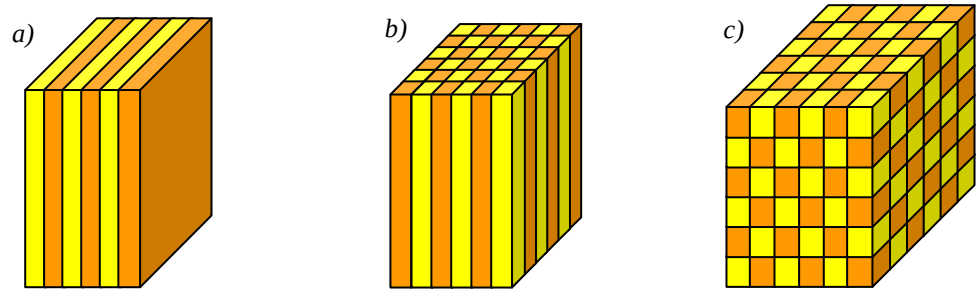

Figure 1.1.1. Periodic electromagnetic media "Photonic Crystals" – a) periodic in one direction (1D), b) periodic in two directions (2D), c) periodic in three directions (3D) [3].

The study of wave propagation in three-dimensionally periodic media was pioneered by Felix Bloch in 1928, extending the theorem in one dimension by G. Floquet (1883). Bloch proved that waves in a periodic medium can propagate without scattering. The field in such medium can be represented by a plane wave multiplied by a periodic envelope function. The band structure of the photonic crystals can be explained using the Bloch theorem.

Starting from the source-free Faraday's and Ampere's laws at a fixed frequency [3] (time dependence $e^{-i\omega t}$), one can obtain an eigenvalue equation in only the magnetic field $\mathbf{H}$:

$$\nabla\times\frac{1}{\varepsilon}\nabla\times\mathbf{H}=\left(\frac{\omega}{c}\right)^2\mathbf{H} \tag{1.1.1}$$

where $\left(\frac{\omega}{c}\right)^2$ is the eigenvalue, $\nabla\times\frac{1}{\varepsilon}\nabla\times$ is the Hermitian eigen-operator, ε is the dielectric function $\varepsilon(\mathbf{r})$, $\mathbf{r}=(x,y,z)$, and c is the speed of light.

A photonic crystal corresponds to a periodic dielectric function $\varepsilon(\mathbf{r})=\varepsilon(\mathbf{r}+\mathbf{R}_i)$ for some primitive lattice vectors $\mathbf{R}_i$ (i = 1, 2, 3 for a crystal periodic in all three dimensions). In this case, the Bloch-Floquet theorem for periodic eigenproblems states that the solutions to equation (1.1.1) can be chosen of the form $\mathbf{H}(\mathbf{r})=e^{i\mathbf{kr}}\mathbf{H}_{n,\mathbf{k}}(\mathbf{r})$ with eigenvalues $\omega_n(\mathbf{k})$, where $\mathbf{k}$ is a Bloch wave vector, and $\mathbf{H}_{n,\mathbf{k}}$ is a periodic envelope function satisfying following equation [3]:

$$(\nabla+i\mathbf{k})\times\frac{1}{\varepsilon}(\nabla+i\mathbf{k})\times\mathbf{H}_{n,\mathbf{k}}=\left(\frac{\omega_n(\mathbf{k})}{c}\right)^2\mathbf{H}_{n,\mathbf{k}} \tag{1.1.2}$$

Equation (1.1.2) gives in effect a different eigenproblem over the primitive cell of the lattice at each Bloch wave vector $\mathbf{k}$. This primitive cell is a finite domain for the structure which is periodic in all directions, leading to discrete eigenvalues labelled by $n = 1, 2, \cdots$. These eigenvalues $\omega_n(\mathbf{k})$ are continuous functions of $\mathbf{k}$, forming discrete "bands" when plotted versus the latter, in a "band structure" or dispersion diagram – both ω and $\mathbf{k}$ are conserved quantities, meaning that a band diagram maps out all possible interactions in the system. The wave vector $\mathbf{k}$ is not required to be real; complex $\mathbf{k}$ gives evanescent modes that can exponentially decay from the boundaries of a finite crystal, but which cannot exist in the bulk.

Moreover, the eigensolutions are periodic functions of $\mathbf{k}$ as well: the solution at $\mathbf{k}$ is the same as the solution at $\mathbf{k} + \mathbf{G}_j$, where $\mathbf{G}_j$ is a primitive reciprocal lattice vector defined by $\mathbf{R}_i \cdot \mathbf{G}_j = 2\pi\delta_{i,j}$. Thus, the computation of the eigensolutions for $\mathbf{k}$ within the primitive cell of the reciprocal lattice is enough to find the eigenvalues of equation (1.1.2). More conventionally, one considers the set of inequivalent wave vectors closest to the $\mathbf{k} = 0$ origin, a region called the first Brillouin zone. For example, in a one-dimensional system, where $\mathbf{R}_1 = a$ for some periodicity a and $\mathbf{G}_1 = 2\pi / a$, the first Brillouin zone is the region $k = -\pi / a \cdots \pi / a$; all other wave vectors are equivalent to some point in this zone under translation by a multiple of $\mathbf{G}_1$. Furthermore, the first Brillouin zone may itself be redundant if the crystal possesses additional symmetries such as mirror planes; by eliminating these redundant regions, one obtains the irreducible Brillouin zone, a convex polyhedron that can be found tabulated for most crystalline structures. In

the preceding one-dimensional example, since most systems will have time-reversal symmetry $(k \to -k)$, the irreducible Brillouin zone would be $k = 0 \cdots \pi / a$ [3].

A complete photonic band gap is a range of frequencies ω in which there are no propagating (real $\mathbf{k}$) solutions of Maxwell's equations (1.1.2) for any $\mathbf{k}$, surrounded by propagating states above and below the gap. There are also incomplete gaps, which only exist over a subset of all possible wave vectors, polarizations, and/or symmetries. The origins for all kinds of the photonic band gap are the same, and can be understood by examining the consequences of periodicity for a simple one-dimensional system.

Considering one-dimensional system with uniform $\varepsilon = 1$, which has planewave eigensolutions $\omega(k) = ck$, and this ε has trivial periodicity a for any $a \geq 0$, with $a = 0$ giving the usual unbounded dispersion relation. One is free, however, to label the states in terms of Bloch envelope functions and wave vectors for some $a \neq 0$, in which case the bands for $|k| > \pi / a$ are translated into the first Brillouin zone, as shown by the dashed lines in figure 1.1.2 b). In particular, the $k = -\pi / a$ mode in this description now lies at an equivalent wave vector to the $k = \pi / a$ mode, and at the same frequency; this accidental degeneracy is an artifact of the "artificial" period chosen. Instead of writing these wave solutions with electric fields $\mathbf{E}(x) \sim e^{\pm i\pi x / a}$, one can equivalently write linear combinations $e(x) = \cos(\pi x / a)$ and $o(x) = \sin(\pi x / a)$ as shown in figure 1.1.3, both at $\omega = c\pi / a$. Now, however, supposing perturbation of ε so that it is nontrivially periodic with period a; for example, a sinusoid $\varepsilon(x) = 1 + \Delta \cdot \cos(2\pi x / a)$, or a square wave as in the inset of figure 1.1.2. In

the presence of such an oscillating "potential," the accidental degeneracy between $e(x)$ and $o(x)$ is broken: supposing $\Delta > 0$, then the field $e(x)$ is more concentrated in the higher-ε regions than $o(x)$, and so lies at a lower frequency. This opposite shifting of the bands creates a band gap, as depicted in figure 1.1.2 b).

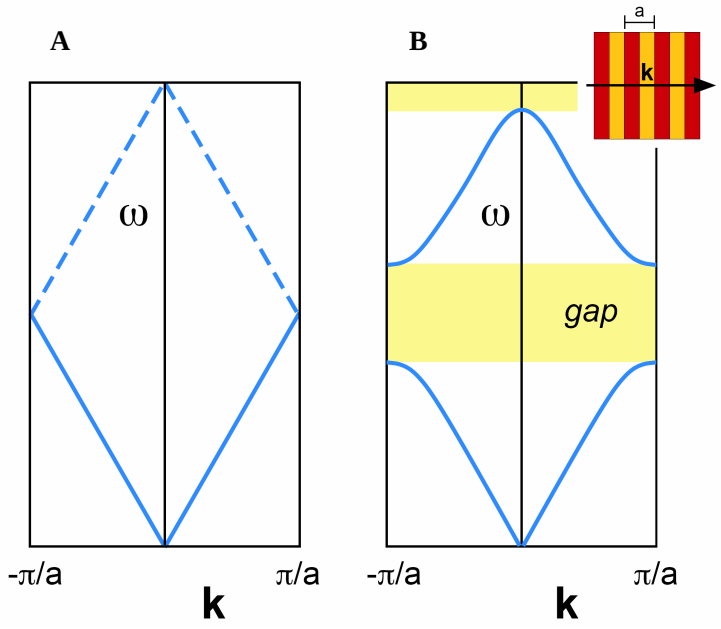

Figure 1.1.2. (a) *Dispersion relation (band diagram), frequency* ω *versus wavenumber* k*, of a uniform one-dimensional medium, where the dashed lines show the "folding" effect of applying Bloch's theorem with an artificial periodicity* a*.* (b) *Schematic effect on the bands of a physical periodic dielectric variation (inset), where a gap has been opened by splitting the degeneracy at the* $k = \pm\pi / a$ *Brillouin-zone boundaries (as well as a higher-order gap at* $k = 0$*)* [3].

By the same arguments, it follows that any periodic dielectric variation in one dimension will lead to a band gap, albeit a small gap for a small variation; a similar result was identified by Lord Rayleigh in 1887. More generally, it follows immediately from the properties of Hermitian eigensystems that the eigenvalues minimize a *variational problem*:

$$\omega_{n,\mathbf{k}}^2 = \min_{\mathbf{E}_{n,\mathbf{k}}} \frac{\int \left|(\nabla + i\mathbf{k}) \times \mathbf{E}_{n,\mathbf{k}}\right|^2}{\int \varepsilon \left|\mathbf{E}_{n,\mathbf{k}}\right|^2} c^2 \qquad (1.1.3)$$

in terms of the periodic electric field envelope $\mathbf{E}_{n,\mathbf{k}}$, where the numerator minimizes the"kinetic energy"and the denominator minimizes the "potential energy". Here, the $n > 1$ bands are additionally constrained to be orthogonal to the lower bands:

$$\int \mathbf{H}_{m,\mathbf{k}}^* \mathbf{H}_{n,\mathbf{k}} = \int \varepsilon \mathbf{E}_{m.\mathbf{k}}^* \mathbf{E}_{n,\mathbf{k}} = 0 \qquad (1.1.4)$$

for $m < n$. Thus, at each $\mathbf{k}$, there will be a gap between the lower "dielectric" bands concentrated in the high dielectric (low potential) and the upper "air" bands that are less concentrated in the high dielectric: the air bands are forced out by the orthogonality condition, or otherwise must have fast oscillations that increase their kinetic energy. (The dielectric/air bands are analogous to the valence/conduction bands in a semiconductor.)

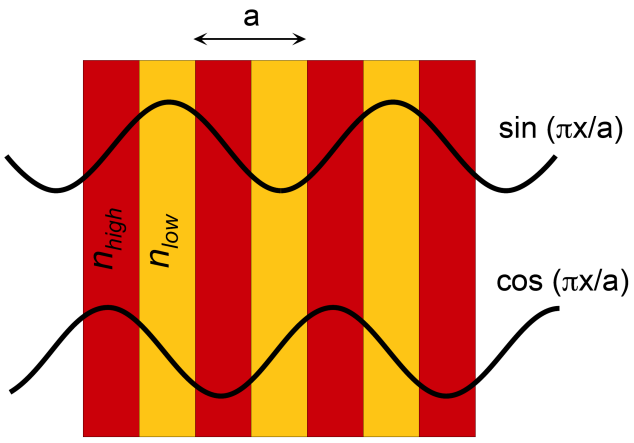

Figure 1.1.3. Schematic origin of the band gap in one dimension. The degenerate $k = \pm\pi/a$ plane waves of a uniform medium are split into $\cos(\pi x/a)$ and $\sin(\pi x/a)$ standing waves by a dielectric periodicity, forming the lower and upper edges of the band gap, respectively – the former has electric field peaks in the high dielectric (n_{high}) and so will lie at a lower frequency than the latter (which peaks in the low dielectric) [3].

In order for a complete band gap to arise in two or three dimensions, two additional hurdles must be overcome. First, although in each symmetry direction of the crystal (and each $\mathbf{k}$ point) there will be a band gap by the one-dimensional argument, these band gaps will not necessarily overlap in frequency (or even lie between the same bands). In order that they overlap, the gaps must be sufficiently large, which implies a minimum ε contrast (typically at least 4/1 in 3D). Since the 1D mid-gap frequency $\sim c\pi / a\sqrt{\bar{\varepsilon}}$ varies inversely with the period *a*, it is also helpful if the periodicity is nearly the same in different directions – thus, the largest gaps typically arise for hexagonal lattices in 2D and fcc lattices in 3D, which have the most nearly circular/spherical Brillouin zones. Second, one must take into account the vectorial boundary conditions on the electric field: moving across a dielectric boundary from ε to some $\varepsilon' < \varepsilon$, the inverse "potential" $\varepsilon|\mathbf{E}|^2$ will decrease discontinuously if $\mathbf{E}$ is parallel to the interface ($\mathbf{E}_{\|}$ is continuous) and will increase discontinuously if $\mathbf{E}$ is perpendicular to the interface ($\varepsilon\mathbf{E}_{\perp}$ is continuous). This means that, whenever the electric field lines cross a dielectric boundary, it is much harder to strongly contain the field energy within the high dielectric, and the converse is true when the field lines are parallel to a boundary. Thus, in order to obtain a large band gap, a dielectric structure should consist of thin, continuous veins/membranes along which the electric field lines can run – this way, the lowest band(s) can be strongly confined, while the upper bands are forced to a much higher frequency because the thin veins cannot support multiple modes (except for two orthogonal polarizations). The veins must also run in all directions, so that this confinement can occur for all $\mathbf{k}$ and polarizations, necessitating a complex topology in the crystal.

1.2. Photonic Crystal Fibres.

Photonic Crystal Fibres PCF's are devices in which the cladding of the conventional fibre was swapped with photonic structure [4][5]. This structures are most two dimensional, in which the cladding is an array of microscopic rods of a material of different refraction index, in most of cases it is a hole filled with air, that run along the entire fibre length. There are also one dimensional structures of the cladding – in this case the fibre is called Bragg PCF, through analogy with Bragg mirror. The process of fabrication of the PCF is very complicated. A general description of the process is shown in figure 1.2.1.

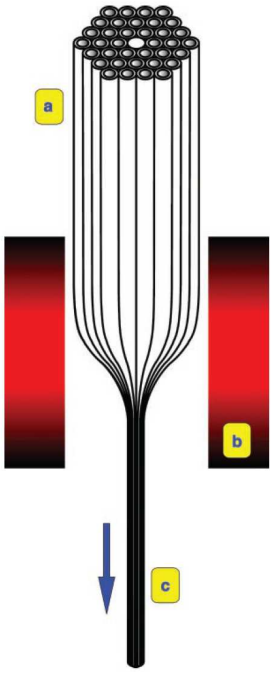

Figure 1.2.1. Manufacturing of the Photonic Crystal Fibres: a) a stack of glass tubes and rods is constructed as a macroscopic "preform" with the required photonic structure, b) the macroscopic structure is fused together and drawn down to a fibre – c)[4].

The geometry of the structure inside the PCF cladding decides about its properties. It was discovered that silica capillaries could be stacked, fused

together, and drawn successfully down to PCF (Fig. 1.2.1). This stack-and-draw procedure proved highly versatile, allowing complex lattices to be assembled from individual stackable units of the correct size and shape. Solid, empty, or doped glass regions could easily be incorporated. Thus, the preform preparation process allows for designing of demanded fibre properties.

The large index contrast and complex structure in PCF make it difficult to treat mathematically. Standard optical fibre analyses do not help, and so Maxwell's equations must be solved numerically. Results are typically presented in the form of a propagation diagram, whose axes are the dimensionless quantities $\beta\Lambda$ and $\omega\Lambda/c$, where Λ is the pitch (interhole spacing) and c is the speed of light in vacuum. This diagram indicates the ranges of frequency and axial wave vector component β where the light is evanescent (unable to propagate). At fixed optical frequency, the maximum possible value of β is set by $kn = \omega n/c$, where n is the refractive index of the region under consideration. For $\beta < kn$, light is free to propagate; for $\beta > kn$, it is evanescent. For conventional fibre (core and cladding refractive indices n_{co} and n_{cl}, respectively), guided modes appear when light is free to propagate in the doped core but is evanescent in the cladding (Fig. 1.2.2 a). The same diagram for PCF is sometimes known as a band-edge or "finger" plot. In a triangular lattice of circular air holes with an air-filling fraction of 45%, light is evanescent in the black regions of Fig. 1.2.2 b). Full two-dimensional photonic band gaps exist within the black fingershaped regions, some of which extend into $\beta < k$ where light is free to propagate in vacuum. This result indicates that hollow-core guidance is indeed possible in the silica-air system. The entire optical telecommunications revolution happened within the narrow strip for

$kn_{cl}\Lambda < \beta\Lambda < kn_{co}\Lambda$ of Fig. 1.2.2 a) (marked with an arrow). The rich variety of new features on the diagram for PCF explains why microstructure Photonic Crystals extend the possibilities of fibres so greatly.

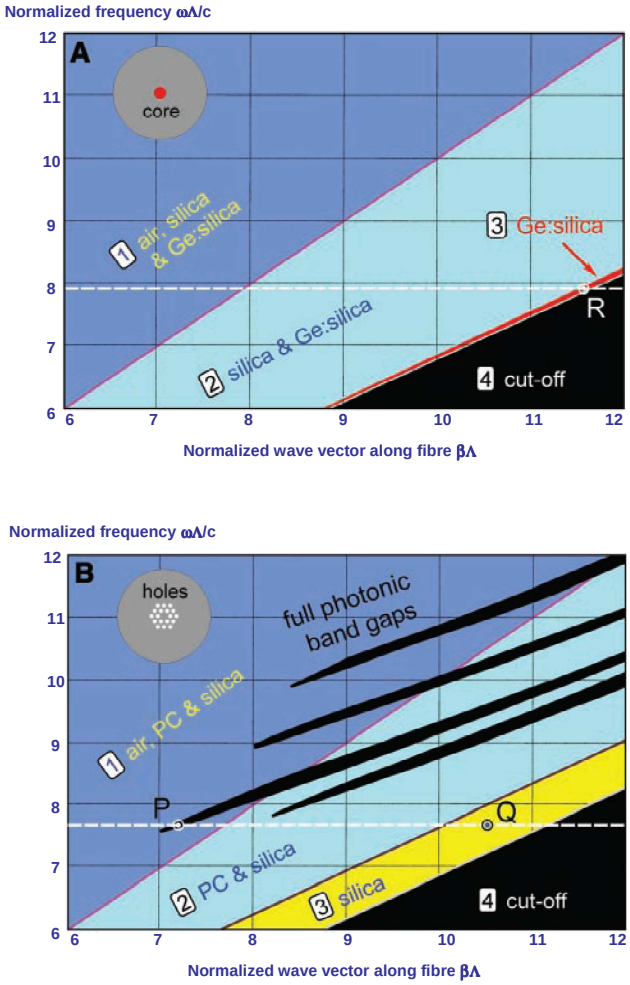

Figure 1.2.2. (a) *Propagation diagram for a conventional single-mode fibre with a Ge-doped silica core and a pure silica cladding.* (b) *Propagation diagram for a triangular lattice of air channels in silica glass with 45% air-filling fraction* [4].

Conventional fibre as presented in the top left corner of the figure 1.2.2 a) is providing guidance due to the total internal reflection phenomena. Guided modes form at points like R, where light is free to travel in the core but unable to penetrate the cladding. The narrow strip marked with 3 in the figure 1.2.2 a) is where the whole of optical telecommunications operates.

Propagation diagram for a triangular lattice of air holes in silica glass with 45% air-filling fraction. In region (1), light is free to propagate in every region of the fibre (air, photonic crystal, and silica). In region (2), propagation is turned off in the air, and, in (3), it is turned off in the air and the PC. In (4), light is evanescent in every region. The black fingers represent the regions where full two-dimensional photonic band gaps exist. Guided modes of a solid core PCF (see schematic in the top left-hand corner, figure 1.2.2 b) form at points such as Q, where light is free to travel in the core but unable to penetrate the PC. At point P, light is free to propagate in air but blocked from penetrating the cladding by the PBG; thus it is possible to design a PCF structure with a hollow core, in which the guidance is provided by the full photonic band gap (hollow-core PCF). This generates the basic classification of the PCFs for the solid core fibres and hollow core fibres with the geometries analogous to this shown on the figure 1.2.3.

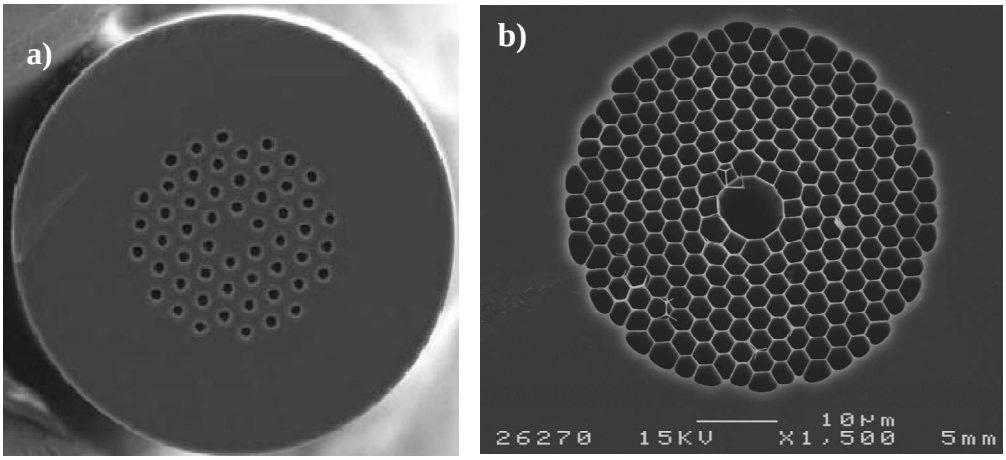

Figure 1.2.3. Basic classification of the PCF: (a) *solid core fibre;* (b) *hollow core fibre* [5].

Earliest numerical models showed that the holes in the first PCF were too small to expect a photonic band gap, and making the hollow core structure was pointless. The air-filling fractions big enough to create full band-gap was

beyond reach in 1995, thus first attempts of creating PCF was solid core structures. Conceptually, it was difficult to determine whether this structure would be a waveguide or not. From one perspective, it resembled a standard fibre because the average refractive index was lower outside the core. By contrast, between the holes there were clear, barrier-free pathways of glass along which light could escape from the core. The answer was provided by the first working photonic crystal fibre (Fig. 1.2.4), which consisted of an array of ~300 nm air holes, spaced 2.3 μm apart, with a central solid core [6]. The striking property of this fibre was that the core did not ever seem to become multimode in the experiments, no matter how short the wavelength of the light, the guided mode always had a single strong central lobe filling the core. This intriguing "endlessly single-mode" behaviour can be understood by viewing the array of holes as a modal filter or "sieve" (Fig. 1.2.5). Because light is evanescent in the air, the holes (diameter d, spacing Λ) act as strong barriers; they are the "wire mesh" of the sieve. The field of the fundamental mode fits into the core with a single lobe of diameter (between zeros) roughly equal to 2Λ. It is the "grain of rice" that cannot escape through the wire mesh because the silica gaps (between the air holes encircling the core) are too narrow. For higher order modes, however, the lobe dimensions are smaller so they can slip between the gaps. As the relative hole size d/Λ is made larger, successive higher order modes become trapped. Correct choice of geometry thus guarantees that only the fundamental mode is guided; more detailed studies show that this occurs for $d/\Lambda < 0.4$ [7]. Very large mode-area fibres become possible, with benefits for high-power delivery, amplifiers, and lasers

[8]. By doping the core to reduce its index slightly, guidance can be turned off completely at wavelengths shorter than a certain threshold value [9].

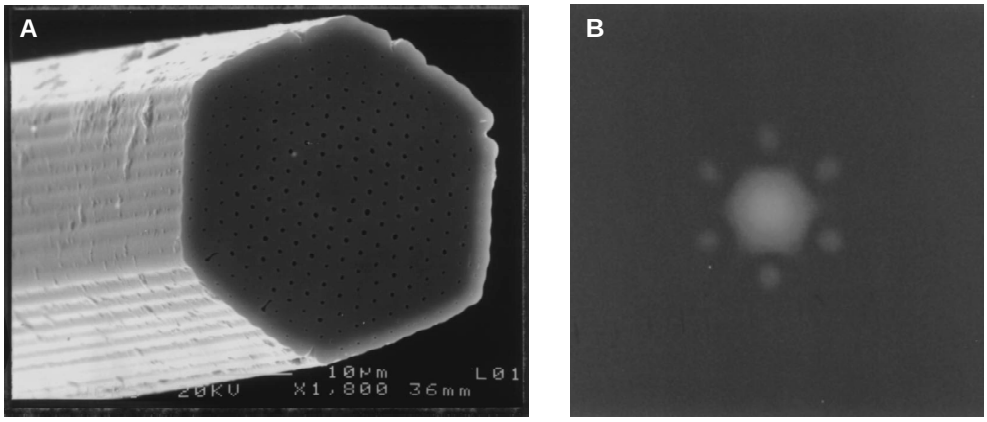

Figure 1.2.4. (a) *Scanning electron micrograph of the first working photonic crystal fibre,* (b) *recorded near-field pattern of the guided mode (λ = 632.8 nm)* [6].

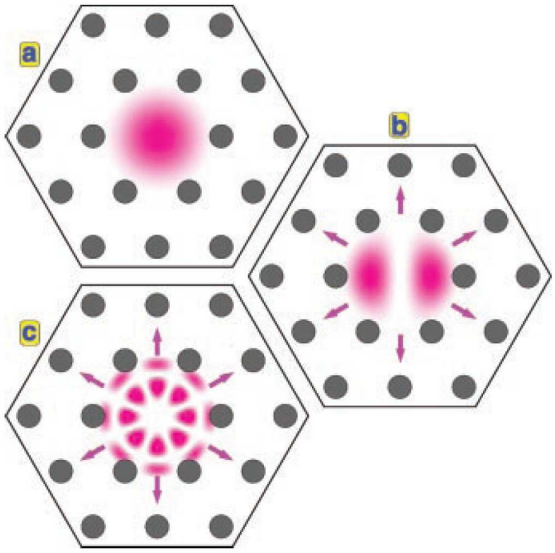

Figure 1.2.5. In a solid-core PCF, the pattern of air holes acts like a modal sieve. In (a), *the fundamental mode is unable to escape because it cannot fit in the gaps between the air holes – its effective wavelength in the transverse plane is too large. In* (b) *and* (c), *the higher order modes are able to leak away because their transverse effective wavelength is smaller. If the diameter of the air holes is increased, the gaps between them shrink and more higher order modes become trapped in the "sieve"*[4].

Hollow-core guidance had to wait until the technology had advanced to the point where larger air-filling fractions, required to achieve a photonic band

gap for incidence from vacuum, became possible. The first such fibre [10] had a simple triangular lattice of holes, and the hollow core was formed by removing seven capillaries (producing a relatively large core that improved the chances of finding a guided mode). A vacuum-guided mode must have $\beta / k < 1$, so the relevant operating region in Fig. 1.2.2 is to the left of the vacuum line, inside one of the finger shaped areas. These conditions ensure that light is free to propagate – and form a mode – within the hollow core while being unable to escape into the cladding. Optical and electron micrographs of a typical hollow-core PCF are shown in Fig. 1.2.6, a) and b). Launching white light into the fibre hollow-core causes them to transmit coloured modes, indicating that guidance existed only in restricted bands of wavelength, coinciding with the photonic band gaps. This feature limits the range of potential applications. More recently it has been possible to greatly widen the transmission bands by fabricating a different structure, a Kagomé lattice [11] (Fig. 1.2.6 c).

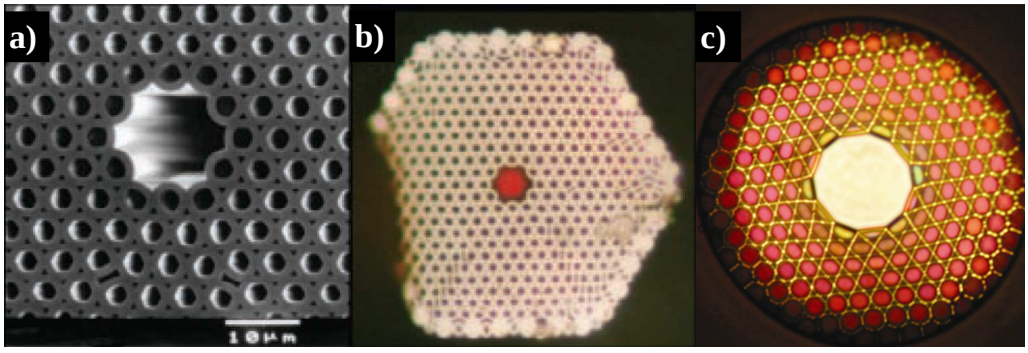

Figure 1.2.6. (a) *SEM of a hollow-core photonic band gap fibre.* (b) *Near-field OM of a red mode in hollow-core PCF (white light is launched into the core).* (c) *OM of a hollow-core PCF with a Kagomé cladding lattice, guiding white light* [11].

Two different guiding mechanisms are presented schematically in figure 1.2.7. In the case of the hollow-core structure, the guidance is possible due to

the Photonic Band-Gap (PBG) of the fibre cladding area. In this case modified total internal reflection, which is deciding in case of solid core fibres, is not possible because the average (effective) refractive index of the cladding area is higher than the refractive index of the core.

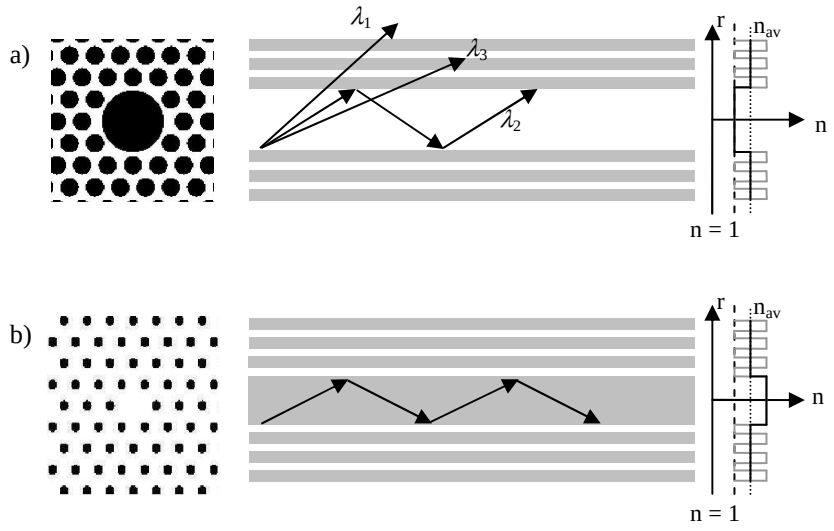

Figure 1.2.7. Guiding mechanisms inside the PCF: (a) *the Photonic Band Gap reflection guiding – the average refraction index of the fibre cladding* n_{av} *is higher than in the core and only the wavelengths of the Photonic Crystal "stopband" can be guided;* (b) *guiding with modified total internal reflection from the cladding area with the average refraction index* n_{av} *lower than in the PCF core.*

Photonic Crystal Fibre offers many new or improved features and finds an increasing number of applications. The ability for design the PCF geometry is also increasing, thus nowadays one can obtain structures with precise defined properties.

Photonic devices can be used as ultra narrow band optic frequencies filters. Hollow-core PCFs (HC-PCFs) finds applications in gas-based nonlinear optics. They allows for maximizing nonlinear interactions between laser light and gases (low-density media). Efficient nonlinear processes require high intensities at low power, long interaction lengths, and good-quality transverse

beam profiles, which HC-PCF offers. Such a fibre finds also applications as the sensing devices for chemicals and for the high harmonic generation (ultraviolet and even x-ray radiation). PCFs with extremely small solid glass cores and very high air-filling fractions not only display unusual chromatic dispersion but also yield very high optical intensities per unit power. Thus one of the most successful applications of PCF is to nonlinear optics, where high effective nonlinearities, together with excellent control of chromatic dispersion, are essential for efficient devices. The example is supercontinuum generation. When ultra-short, high-energy pulses travel through a material, their frequency spectrum can experience giant broadening due to a range of interconnected nonlinear effects.

1.3. New frontiers in photonic optical technologies.

Photonic devices and photonics is a research area which development is very fast and efficient nowadays. Such devices find application in almost every scientific area. Recent advances in this emerging area now enable to launch a systematic approach toward the goal of full systems-level integration. The most important goal is to integrate photonics with nanotechnology and developing novel photonic devices. The technology of the fabrication of photonic structures, for example Molecular Beam Epitaxy, allows for production of photonic nanomaterials and sub-wavelength devices. Although incomplete understanding of the interactions between light and photonic nanostructures, the physics and technology of sub-wavelength structured optical materials such as photonic crystals, patterned metallic films and, more generally, artificial optical materials, such as metamaterials (i.e. structured materials with new characteristics obtained by combining materials properties

and geometrically patterning), offer novel phenomena and applications – mainly because of their unique dispersion characteristics, which include photonic band-gap behaviour and slow propagation of light.

This research area still needs a lot of work for full integration of light with nano-scale devices and processes, as well as dynamic and all-optical control of nanostructures. The associated strong optical confinement has already led to much more compact devices and enhanced non-linear effects, implying the possible replacement of electronic functionality by all-optical operation at the highest speeds. There is an extensive worldwide effort, in both academic and commercial research labs, to address these challenges.

2. Introduction to the numerical methods used in the developed program.

The range of applications for photonic devices is very wide. The properties of the photonic structures allows for the creation of devices with specified, demanded characteristics. However the cost of manufacturing of such structures is very high and involves advanced technology. Manufacturing and testing of the devices to check the influence of different parameters of the structure for its properties will be extremely expensive and will consume a lot of time. Thus it is better to “predict” the characteristics of the designed device with analytical calculations.

Photonic crystal, in most cases is a complicated structure; which characteristic does not have strict analytical solution. This is the area for a well prepared analytical model combined with numerical methods to find approximated solution.

2.1. Theory – short introduction.

The starting point is the classical set of the Maxwell equations in differential form:

$$\begin{cases} rot\mathbf{H} - \dfrac{\partial \mathbf{D}}{\partial t} = 0 \\ rot\mathbf{E} + \dfrac{\partial \mathbf{B}}{\partial t} \end{cases}, \qquad \begin{cases} div\mathbf{D} = 0 \\ div\mathbf{B} = 0 \end{cases} \tag{2.1.1}$$

H – vector of the magnetic field,

D – electric field induction vector,

B – magnetic induction vector,

E – vector of the electric field.

Material equations:

$$\begin{cases} \mathbf{D} = \varepsilon\varepsilon_0\mathbf{E} \\ \mathbf{B} = \mu\mu_0\mathbf{H} \end{cases} \tag{2.1.2}$$

ε – electric permeability of the medium,

ε_0 – electric permeability of the vacuum,

μ – magnetic permeability of the medium,

μ_0 – magnetic permeability of the vacuum.

The vectorial wave equation for the isotropic medium without the charges and free currents (dielectric), assuming the field proportional to $\sim e^{-i\omega t}$, is [12]:

$$\Delta\mathbf{E} + n^2k^2\mathbf{E} = \nabla\left(\nabla\mathbf{E}\right) \tag{2.1.3}$$

where: n is the refraction index of the medium, k is the wavevector of the considered beam. For the propagation in one direction without reflections (assuming z-axis direction), only two transverse field components (E_x, E_y) are needed to characterize the field. Assuming small angle discrepancy of the beam

(true inside the optical fibre) and slowly varying refraction index along the propagation axis, the equation (2.1.3) can be derived to the following form [12]:

$$\nabla_t \mathbf{E}_t + (n^2 - {n_0}^2)k^2\mathbf{E}_t - \nabla_t[\nabla_t\mathbf{E}_t - \frac{1}{n^2}\nabla_t(n^2\mathbf{E}_t)] = 2in_0k\frac{\partial\mathbf{E}_t}{\partial z} \qquad (2.1.4)$$

where n_0 is the reference refraction index, and index t denotes the transverse field component (x or y).

Assumptions made in this section allow for faster calculations and less memory consumption in every step of the developed algorithm. These assumptions also bring some disadvantages, such as ignoring backward reflections and impossibility of simulations of the wide angle beam propagation.

2.2. Implementation of the method in FORTRAN.

The calculation area is limited in space and discretized. The developed code discretizes the calculation area with a regular, rectangular mesh of points shown in figure 2.2.1. Assuming distances between the calculation points Δx in the x-axis direction and Δy in the y-axis direction, an arbitrary point $P_{i,j}$ is described with the co-ordinates ($i \cdot \Delta x$, $j \cdot \Delta y$). The rectangular mesh is very easy to implement in the code, however for accurate calculations it should be dense. Dense mesh allows for making the staircasing effect smaller, but it utilizes much more calculations. The staircasing effect is occurs because the outer boundary of an object of an arbitrary geometry does not conform to the rectangular mesh in described method. The effect is shown in figure 2.2.2. The real shape of an object is represented by finished number of the point samples. As it can be observed in figure 2.2.2, using mesh with higher density (Fig. 2.2.2 b) allows for more accurate representation of the physical object in

the algorithm, thus also for describing more complex geometries of the simulated structure.

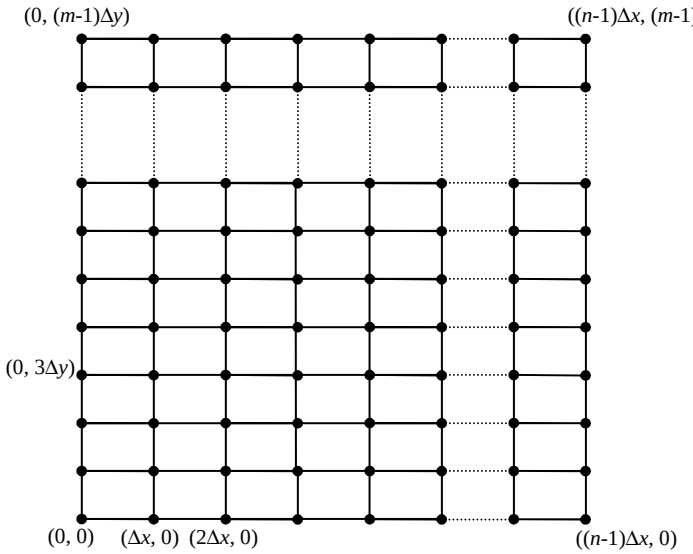

Figure 2.2.1. Rectangular, regular mesh of discretization used in the developed code.

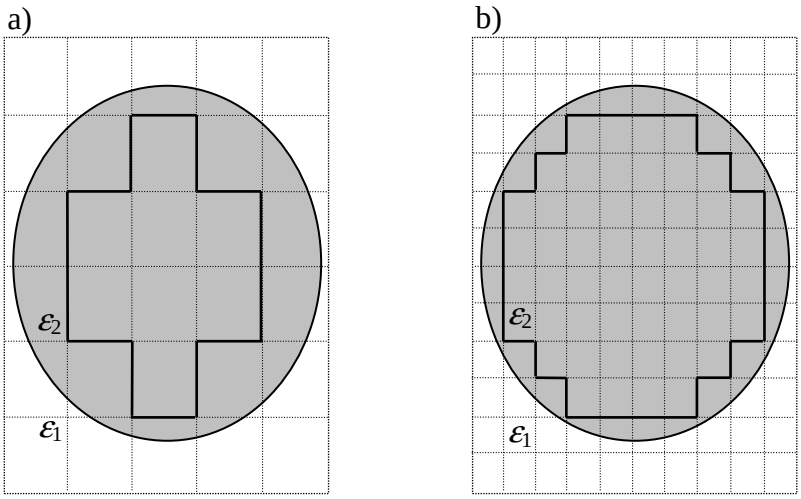

Figure 2.2.2. The staircasing effect – the area marked with lines is the representation of the elliptic shaped object (electric permeability ε_2) discretized with a mesh with different density. The finer mesh allows for distretizing more complex structures with greater accuracy.

Typical PCF is a complex structure containing circle shaped holes inside the cladding area. For the description of such a structure with a rectangular mesh, it is necessary to use adequately dense mesh of points.

After a structure is discretiyed, the equation (2.1.4) must be solved in this structure at the propagation length *z*. For a complex structure (like PCF), the analytical solution is impossible to obtain. The presented code is using Beam Propagation Method with the differentials in equation (2.1.4) replaced by the following formulas [12]:

$$\begin{cases} \dfrac{\partial F^{i,j}}{\partial x} = \dfrac{F^{i+1,j} - F^{i-1,j}}{2\Delta x}, & \dfrac{\partial^2 F^{i,j}}{\partial x^2} = \dfrac{F^{i+1,j} - 2F^{i,j} + F^{i-1,j}}{(\Delta x)^2} \\ \dfrac{\partial F^{i,j}}{\partial y} = \dfrac{F^{i,j+1} - F^{i,j-1}}{2\Delta y}, & \dfrac{\partial^2 F^{i,j}}{\partial y^2} = \dfrac{F^{i,j+1} - 2F^{i,j} + F^{i,j-1}}{(\Delta y)^2} \end{cases} \tag{2.2.1}$$

This is so called Finite-Difference Scheme. After substitution of (2.2.1) into (2.1.4) and after derivation, the set of equations for two elements of the electric field vector E_x and E_y [13,14]:

$$\begin{aligned} &\alpha \mathbf{a}_x^{i,j,s+1} E_x^{i-1,j,s+1} + \alpha \mathbf{b}_x^{i,j,s+1} E_x^{i,j-1,s+1} + \left[1 + \alpha \mathbf{c}_x^{i,j,s+1}\right] E_x^{i,j,s+1} + \\ &\qquad + \alpha \mathbf{b}_x^{i,j,s+1} E_x^{i,j+1,s+1} + \alpha \mathbf{g}_x^{i,j,s+1} E_x^{i+1,j,s+1} = \\ &= -\beta \mathbf{a}_x^{i,j,s} E_x^{i-1,j,s} - \beta \mathbf{b}_x^{i,j,s} E_x^{i,j-1,s} + \left[1 + \beta \mathbf{c}_x^{i,j,s}\right] E_x^{i,j,s} - \beta \mathbf{b}_x^{i,j,s} E_x^{i,j+1,s} - \beta \mathbf{g}_x^{i,j,s} E_x^{i+1,j,s} + \\ &\qquad + \mathbf{h}_x^{i,j,s} E_y^{i-1,j,s} - \mathbf{m}_x^{i,j,s} E_y^{i,j,s} - \mathbf{h}_x^{i,j,s} E_y^{i+1,j,s} \end{aligned} \tag{2.2.2}$$

parameter α used in the equations is the parameter responsible for the calculation scheme – implicit-explicit; and determines the stability of the algorithm, *s* is the step number in the direction of *z*-axis, and other parameters are defined with formulas:

$$\mathbf{a}_x^{i,j,s} = \frac{i\Delta z}{4 n_0 k} \left[\frac{1}{(\Delta x)^2} - \frac{1}{n^{i,j,s}} \frac{n^{i+1,j,s} - n^{i-1,j,s}}{2(\Delta x)^2} \right] \tag{2.2.3}$$

$$\mathbf{b}_x^{i,j,s} = \frac{i\Delta z}{4 n_0 k} \frac{1}{(\Delta y)^2} \tag{2.2.4}$$

$$\mathbf{c}_x^{i,j,s} = \frac{i\Delta z}{n_0 k}\left[\frac{-\left(n^{i+1,j,s}-n^{i-1,j,s}\right)^2}{2\Delta x n^{i+1,j,s}n^{i-1,j,s}}+\frac{2\left(n^{i+1,j,s}-n^{i,j,s}+n^{i-1,j,s}\right)}{n^{i,j,s}\left(\Delta x\right)^2}\right]+$$
$$+\frac{i\Delta z}{n_0 k}\left[-2\left(\frac{1}{\left(\Delta x\right)^2}+\frac{1}{\left(\Delta y\right)^2}\right)+\left(\left(n^{i,j,s}\right)^2-n_0^2\right)k^2\right] \tag{2.2.5}$$

$$\mathbf{g}_x^{i,j,s} = \frac{i\Delta z}{4n_0 k}\left[\frac{1}{\left(\Delta x\right)^2}+\frac{1}{n^{i,j,s}}\frac{n^{i+1,j,s}-n^{i-1,j,s}}{2\left(\Delta x\right)^2}\right] \tag{2.2.6}$$

$$\mathbf{h}_x^{i,j,s} = \frac{i\Delta z}{4n_0 k}\left[\frac{1}{n^{i,j,s}}\frac{n^{i,j+1,s}-n^{i,j-1,s}}{\Delta x\Delta y}\right] \tag{2.2.7}$$

$$\mathbf{m}_x^{i,j,s} = \frac{i\Delta z}{4n_0 k}\left[\frac{\left(n^{i-1,j,s}-n^{i+1,j,s}\right)\left(n^{i,j+1,s}-n^{i,j-1,s}\right)}{2\Delta x\Delta y n^{i-1,j,s}n^{i+1,j,s}}\right]+$$
$$+\frac{i\Delta z}{4n_0 k}\left[\frac{\left(n^{i+1,j+1,s}-n^{i-1,j+1,s}-n^{i+1,j-1,s}+n^{i-1,j-1,s}\right)}{2\Delta x\Delta y n^{i,j,s}}\right] \tag{2.2.8}$$

The equation for the field component E_y is:

$$\alpha\mathbf{a}_y^{i,j,s+1}E_y^{i,j-1,s+1}+\alpha\mathbf{b}_y^{i,j,s+1}E_y^{i-1,j,s+1}+\left[1+\alpha\mathbf{c}_y^{i,j,s+1}\right]E_y^{i,j,s+1}+$$
$$+\alpha\mathbf{b}_y^{i,j,s+1}E_y^{i+1,j,s+1}+\alpha\mathbf{g}_y^{i,j,s+1}E_y^{i,j+1,s+1}=$$
$$=-\beta\mathbf{a}_y^{i,j,s}E_y^{i,j-1,s}-\beta\mathbf{b}_y^{i,j,s}E_y^{i-1,j,s}+\left[1+\beta\mathbf{c}_y^{i,j,s}\right]E_y^{i,j,s}-\beta\mathbf{b}_y^{i,j,s}E_y^{i+1,j,s}-\beta\mathbf{g}_y^{i,j,s}E_y^{i,j+1,s}+$$
$$+\mathbf{h}_y^{i,j,s}E_x^{i,j-1,s}-\mathbf{m}_y^{i,j,s}E_x^{i,j,s}-\mathbf{h}_y^{i,j,s}E_x^{i,j+1,s} \tag{2.2.9}$$

where:

$$\beta = 1-\alpha \tag{2.2.10}$$

$$\mathbf{a}_y^{i,j,s} = \frac{i\Delta z}{4n_0 k}\left[\frac{1}{\left(\Delta y\right)^2}-\frac{1}{n^{i,j,s}}\frac{n^{i,j+1,s}-n^{i,j-1,s}}{2\left(\Delta y\right)^2}\right] \tag{2.2.11}$$

$$\mathbf{b}_y^{i,j,s} = \frac{i\Delta z}{4n_0 k}\frac{1}{\left(\Delta x\right)^2} \tag{2.2.12}$$

$$\mathbf{c}_y^{i,j,s} = \frac{i\Delta z}{n_0 k}\left[\frac{-\left(n^{i,j+1,s} - n^{i,j-1,s}\right)^2}{2\Delta y n^{i,j+1,s} n^{i,j-1,s}} + \frac{2\left(n^{i,j+1,s} - n^{i,j,s} + n^{i,j-1,s}\right)}{n^{i,j,s}\left(\Delta y\right)^2}\right] + \\ + \frac{i\Delta z}{n_0 k}\left[-2\left(\frac{1}{\left(\Delta x\right)^2} + \frac{1}{\left(\Delta y\right)^2}\right) + \left(\left(n^{i,j,s}\right)^2 - n_0^2\right)k^2\right] \tag{2.2.13}$$

$$\mathbf{g}_y^{i,j,s} = \frac{i\Delta z}{4n_0 k}\left[\frac{1}{\left(\Delta y\right)^2} + \frac{1}{n^{i,j,s}}\frac{n^{i,j+1,s} - n^{i,j-1,s}}{2\left(\Delta y\right)^2}\right] \tag{2.2.14}$$

$$\mathbf{h}_y^{i,j,s} = \frac{i\Delta z}{4n_0 k}\left[\frac{1}{n^{i,j,s}}\frac{n^{i+1,j,s} - n^{i-1,j,s}}{\Delta x \Delta y}\right] \tag{2.2.15}$$

$$\mathbf{m}_y^{i,j,s} = \frac{i\Delta z}{4n_0 k}\left[\frac{\left(n^{i,j-1,s} - n^{i,j+1,s}\right)\left(n^{i+1,j,s} - n^{i-1,j,s}\right)}{2\Delta x \Delta y n^{i,j-1,s} n^{i,j+1,s}}\right] + \\ + \frac{i\Delta z}{4n_0 k}\left[\frac{\left(n^{i+1,j+1,s} - n^{i+1,j-1,s} - n^{i-1,j+1,s} + n^{i-1,j-1,s}\right)}{2\Delta x \Delta y n^{i,j,s}}\right] \tag{2.2.16}$$

Thus, if the number of point in *x*-axis direction is M, and the number of points in the *y*-axis direction is N, a set of $2 \cdot M \cdot N$ equations is obtained. $M \cdot N$ equations for E_x component, and the same number for E_y component. This set of equations can be rewritten in the matrix form:

$$E_x^{s+1} = \left[\mathbf{M}_x\right]^{-1}\left(\left[\mathbf{N}_x\right]E_x^s + \left[\mathbf{Q}_{xy}\right]E_y^s\right) \tag{2.2.17}$$

$$E_y^{s+1} = \left[\mathbf{M}_y\right]^{-1}\left(\left[\mathbf{N}_y\right]E_y^s + \left[\mathbf{Q}_{yx}\right]E_x^s\right) \tag{2.2.18}$$

where **M**, **N**, **Q** are the tri-diagonal matrices containing coefficients for each calculated point, E_x and E_y represent two components of the electric field vector. The electric field in the next step ($s+1, z_{s+1} = z_s + h$, where h is the step size) is calculated with the use of the field distribution known from

the previous step (s, z_s). The scheme of solving equations showed above is stable for $\alpha \geq 0.5$.

2.3. Boundary Conditions.

Due to limitations in computations efficiency the simulated structure must have finite dimensions. To avoid non-physical effects e.g. reflections from the boundary surface there is need to use an additional scheme which removes this effect. The field reflected at the boundary surface can interfere with the propagating field and affect the calculations results. This situation occurs for the Dirichlet boundary conditions ($E = 0$ at the boundary surface), or for the Noumann boundary conditions (derivative of the field E is 0 at the boundary surface). In order to avoid non-physical interference effect of the signal reflected at the boundary surface, the Transparent Boundary Conditions was used.

The field described with equation (2.1.4) at the boundary surface with the homogenous refractive index distribution can be derived to the formulas [15]:

$$\frac{\partial E_x}{\partial z} = \frac{1}{2ikn_0}\left(\frac{\partial}{\partial x^2}E_x + \frac{\partial}{\partial y^2}E_x\right) \tag{2.3.1}$$

$$\frac{\partial E_y}{\partial z} = \frac{1}{2ikn_0}\left(\frac{\partial}{\partial x^2}E_y + \frac{\partial}{\partial y^2}E_y\right) \tag{2.3.2}$$

Introducing equation conjugated to (2.3.1):

$$\frac{\partial E_x^*}{\partial z} = \frac{1}{2ikn_0}\left(\frac{\partial}{\partial x^2}E_x^* + \frac{\partial}{\partial y^2}E_x^*\right) \tag{2.3.3}$$

and multiplying the equation (2.3.1) by E_x^* and (2.3.3) by E_x, and adding both sides of the obtained equations, one can describe the energy preservation law in the form:

$$\frac{\partial}{\partial z}\int_a^b\int_c^d |E_x|^2 dxdy = \\ = \frac{1}{2ikn_0}\left[\int_c^d\left(\left(E_x^*\frac{\partial}{\partial x}E_x - E_x\frac{\partial}{\partial x}E_x^*\right)\Big|_a^b\right)dy + \int_a^b\left(\left(E_y^*\frac{\partial}{\partial y}E_y - E_y\frac{\partial}{\partial y}E_y^*\right)\Big|_c^d\right)dx\right] = \\ = (F_b - F_a) + (F_d - F_c) \tag{2.3.4}$$

where *a* and *b* are respectively the beginning and the end of the calculation area in the *x*-axis direction, *c* and *d* are respectively the beginning and the end of the calculation area in the *y*-axis direction. F_a and F_b are the energy streams through the boundary surface in the *x*-axis direction, F_c and F_d are the energy streams through the boundary surface in the *y*-axis direction. At the boundary of the calculation window, the field can be approximated with the following expression:

$$E_x = E_0 \exp(ik_x x + ik_y y) \tag{2.3.5}$$

where E_0, k_x, and k_y are the complex constants. This is the assumption of the outgoing field to be a plane wave. Derivation of (2.3.5) into (2.3.4) gives in result the following equations describing the energy streams floating through the calculation window boundary surface:

$$F_a = \frac{\mathrm{Re}(k_{xa})|E_x(a)|^2}{k_0 n_0}, \quad F_b = \frac{\mathrm{Re}(k_{xb})|E_x(b)|^2}{k_0 n_0} \tag{2.3.6}$$

$$F_c = \frac{\mathrm{Re}(k_{xc})|E_x(c)|^2}{k_0 n_0}, \quad F_d = \frac{\mathrm{Re}(k_{xd})|E_x(d)|^2}{k_0 n_0} \tag{2.3.7}$$

Thus the energy stream depends on the real part of the k_x. Considering the set of equations (2.3.6) and (2.3.7) one can notice, that the positive sign of the k_{xa} value means the outgoing energy stream F_a (k_{xa} is the value of k_x near the boundary *a*). When the sign of the k_{xa} value is positive – the energy stream F_a is incoming to the calculation window, which should be rejected as a non-physical case. The code controls k_x at the boundary, and prevents this non-physical behaviour.

Differential form of the boundary conditions presented above is following:

$$\frac{E_x^{2,j,s}}{E_x^{3,j,s}} = \frac{E_x^{1,j,s}}{E_x^{2,j,s}} = \exp(ik_{xa}\Delta x) \tag{2.3.8}$$

$$\frac{E_x^{M-1,j,s}}{E_x^{M-2,j,s}} = \frac{E_x^{M,j,s}}{E_x^{M-1,j,s}} = \exp(ik_{xb}\Delta x) \tag{2.3.9}$$

$$\frac{E_x^{i,2,s}}{E_x^{i,3,s}} = \frac{E_x^{i,1,s}}{E_x^{i,2,s}} = \exp(ik_{xc}\Delta x) \tag{2.3.10}$$

$$\frac{E_x^{i,N-1,s}}{E_x^{i,N-2,s}} = \frac{E_x^{i,N,s}}{E_x^{i,N-1,s}} = \exp(ik_{xd}\Delta x) \tag{2.3.11}$$

where M is the number of points in the *x*-axis direction, and N is the number of points in the *y*-axis direction. The estimation of the field at the boundary surface in the next step of propagation:

$$E_x^{1,j,s+1} = E_x^{2,j,s+1}\left(\frac{E_x^{2,j,s}}{E_x^{3,j,s}}\right) \tag{2.3.12}$$

$$E_x^{M,j,s+1} = E_x^{M-1,j,s+1}\left(\frac{E_x^{M-1,j,s}}{E_x^{M-2,j,s}}\right) \tag{2.3.13}$$

$$E_x^{i,1,s+1} = E_x^{i,2,s+1}\left(\frac{E_x^{i,2,s}}{E_x^{i,3,s}}\right) \tag{2.3.14}$$

$$E_x^{i,N,s+1} = E_x^{i,N-1,s+1}\left(\frac{E_x^{i,N-1,s}}{E_x^{i,N-2,s}}\right) \tag{2.3.15}$$

Thus the boundary conditions in (s + 1) step are calculated in the previous s step. Using scheme described above allows for setting the transparent boundaries at the ends of the calculation window.

2.4. Nonlinear effects.

Dielectric media characterizes with lack of the free charges which could be moving in ordered way by the influence of the external electrical field $\mathbf{E} = \left(E_x, E_y, E_z\right)$. Summarized charge of the dielectric particle is equal zero, nevertheless it is interact with the electric field. Assuming Transverse Electric (TE) field in a scalar approximation, when only one of the $\mathbf{E}$ field components need to be considered, i.e. $E_x = E\left(x,t\right) = A\exp\left(ikx - i\omega t\right)$, considering monochromatic field which amplitude A is constant in time and space, the polarization of the dielectric is represented with formula:

$$P = \varepsilon_0 \chi A \tag{2.4.1}$$

where ε_0 is the vacuum electric permeability, χ is the electric susceptibility of the medium. Equation (2.4.1) describes the linear dependence between the electric field and the medium. In general dielectric polarization contains higher order components, and is nonlinear function of the electric field A [16]:

$$P = \varepsilon_0\left[\chi^{(1)}A + \chi^{(2)}A^2 + \chi^{(3)}A^3 + ...\right] = \varepsilon_0\left[\chi^{(1)} + \chi^{(2)}A + \chi^{(3)}A^2 + ...\right]A \tag{2.4.2}$$

Dependence of the polarization value of the external fields causes modification of the material electric permeability, and also its refraction index. Considering

the polarization described by expression (2.4.2) one can obtain the electric induction D described by following expression:

$$D = \varepsilon_0 A + \varepsilon_0 \left[\chi^{(1)} + \chi^{(2)} A + \chi^{(3)} A^2 + ... \right] A = \varepsilon_0 \left[1 + \chi^{(1)} + \chi^{(2)} A + \chi^{(3)} A^2 + ... \right] A \tag{2.4.3}$$

In general $D = \varepsilon(\omega) A$, and considering non-magnetic media $(\mu = 1)$, thus $n = n(\omega) = \sqrt{\mu\varepsilon} = \sqrt{\varepsilon}$, and in effect, after discarding higher order components, one can obtain the value of the mediums refraction index described with formula:

$$n = \sqrt{1 + \chi^{(1)} + \chi^{(2)} A + \chi^{(3)} A^2} \tag{2.4.4}$$

The linear part (field independent) of the total refraction index value can be described with expression:

$$n_0 = n_0(\omega) = \sqrt{1 + \chi^{(1)}} \tag{2.4.5}$$

assuming that the considered medium is isotropic in which nonlinearities of even order does not appear, total value of the refraction index can be described with:

$$n = n_0 \sqrt{1 + \chi^{(3)} A^2 / n_0^2} \tag{2.4.6}$$

The root expression can be represented with the Taylor series with respect to $\chi^{(3)} A^2$ (assuming $\chi^{(3)} A^2 << n_0$). Discarding the higher order expressions one can obtain following formula:

$$n \approx n_0 + n_{NL} I \text{, where } I \sim |A|^2 \tag{2.4.7}$$

where nonlinear part of the refractive index is defined as $n_{NL} = \chi^{(3)} / 2n_0$, and I is the intensity of the electromagnetic wave. Definition (2.4.7) describes

the dependence of the total refractive index on the intensity of the propagating field. It means that the field self modifies the properties of the medium without external effects. Nonlinear Kerr effect provides additional impact on the beam propagation. The most interesting is the effect of self focusing, which in specific conditions can result in formation of the spatial soliton when the self focusing compensates the effect of diffraction widening.

2.5. Split-Step Local Error Method.

Introducing nonlinearity to the computations brings additional effects, including the modification of the refractive index with the beam intensity value (in case of Kerr nonlinearity, which is performed in presented algorithm). For minimization of the disadvantageous effects the Split-Step Local Error Method (LEM) was added to the algorithm.

Each step of the numerical computations generates an error which is the effect of simplifications used, or of the specification of the problem. This error is so called local error. One of the methods used for minimization of this error are Split-Step methods. The exact value of the local error is impossible to determine, however the causes of this error are possible to define with high accuracy. Split-Step Methods are used for partial elimination of the local error through elimination of the main cause of its generation. However, when this cause cannot be defined precisely or in case when the group of the parameters of performed calculations can be changed in the algorithm, particular models cannot be used. This is the main reason for creation of some general criterion for the Split-Step algorithm. An interesting solution is presented by Sinkin in [17]. The proposed algorithm allows for bounding the local error value in a specified range with use of double step and extrapolation of the local error

value. Assuming field distribution known at the z surface, the field at the $z+2h$ can be estimated (h is the length of single step in the z-axis direction). This is realized with computations of the field in $z+2h$ with use of one calculation step of $2h$ length. The solution obtained this way is named *coarse* solution e_c. The error generated is proportional to h^3, thus there is a constant κ for which is true that:

$$e_c = e_t + \kappa(2h)^3 + O\left(h^4\right) \tag{2.5.1}$$

where e_t is real value of the field at $z+2h$, $O\left(h^4\right)$ are the higher order components. Next the computations are repeated from z to $z+2h$ with use of two steps of h size. Obtained result is named *fine* solution e_f, which satisfies the expression:

$$e_f = e_t + 2\kappa h^3 + O\left(h^4\right) \tag{2.5.2}$$

By taking an appropriate linear combination of the fine and coarse solutions an approximate solution at $z+2h$ can be obtained, for which the leading order error term is of fourth order in the step size h. From the expressions (2.5.1) and (2.5.2) the expression can be obtained:

$$E = \frac{4}{3}e_f - \frac{1}{3}e_c = e_t + O\left(h^4\right) \tag{2.5.3}$$

Used scheme allows for bounding the local error value within a specified range, determined by the user. The true value of the local error is impossible to determine. Instead, the relative local error of a step σ can be defined, to be the local error in the coarse solution relative to the fine solution. In case of presented algorithm the relative local error is defined with:

$$\sigma = \sqrt{\frac{\sum_{i,j=1}^{M,N}\left[e_f(i,j) - e_c(i,j)\right]^2}{\sum_{i,j=1}^{M,N}\left[e_f(i,j)\right]^2}}, \qquad (2.5.4)$$

where: M – is the total number of grid points along the x axis, N – is the total number of grid points along the y axis, $e_f(i,j), e_c(i,j)$ – are the fine and coarse field intensity value in grid point (i,j), respectively. Equation (2.5.4) gives the mean quadratic deviation of the fine and coarse solution.

The step size is chosen by keeping the relative local error value σ in the specified range $(1/2\sigma_G, \sigma_G)$, determined by a fixed value σ_G – the goal local error. If $\sigma > 2\sigma_G$ – the obtained solution is discarded and step size is halved, the computations are repeated one more time. If σ is in the range $(\sigma_G, 2\sigma_G)$; the step size is divided by a factor of $2^{1/3}$ for the next step. If $\sigma < 1/2\sigma_G$, the step size is multiplied by a factor of $2^{1/3}$ for the next step. Field distribution obtained from equation (2.5.3) is the input for next step computations.

2.6. Description of the algorithm.

Program uses two input files containing parameters of the input Gaussian beam and the characteristics of the propagation medium including characteristics of the computational window. File called *structureKerr.txt* contains the values defining the structure in which the beam propagates. The code of the developed program is written to generate structure shown on the figure 2.6.1. Algorithm is creating the hexagonal lattice and the input file contains the values of the diameter of the holes, the period of the lattice, refractive index of

the dielectric and the refractive index inside the holes, Kerr coefficient and the number of the hole rings surrounding the solid core. Other modifications of the structure demands changes in the algorithm defining the structure.

The file named *config.txt* contains the computational window size and mesh resolution, propagation length, propagation step size Δz, propagation length section, in which the output data is saved to the file, the reference refractive index, the wavelength, the Gaussian beam width parameter, the value of the goal local error, the field incident angle in degrees and the proportion between the *x* and *y* component of the field. Three files generated in equal division of propagation length containing the intensity of the *x* component, y component and the beam intensity respectively.

Results of the computation are written into three text output files: the first two files contain the components of the field E_x, E_y and the third one contains the module of the field $\left|E^2\right| = \sqrt{E_x^2 + E_y^2}$. These three files are saved several times for equal segments of the propagation length. Next, the obtained data files are used to plot the field distribution with the use of GnuPlot program.

The example of the index distribution across the fibre under investigation is shown in the figure 2.6.1. Basic parameters of that structure can be easily modified in the input text file.

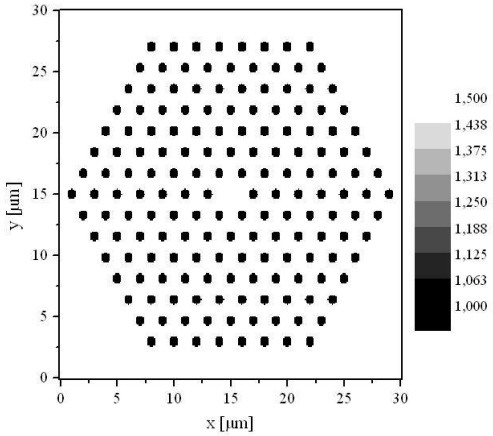

Figure 2.6.1. Example of the refractive index distribution inside the simulated fibre (hexagonal lattice photonic structure in the cladding area).

The code of the developed program allows for generating the structure shown above. To change the geometry of this structure, one needs to change the code of the program.

3. Validation of the developed code.

In order to validate the developed FD-BPM code the results obtained from the simulations were first checked against analytical results for linear propagation in free space. The comparison was made for different propagation lengths and different wavelengths.

The field distribution of the Gaussian beam is calculated with the formula:

$$E(r,z) \sim E_0\left(\frac{w_0}{w(z)}\right)\exp\left(\frac{-r^2}{w^2(z)}\right), \text{ where } w(z) = w_0\sqrt{1+(z/z_0)^2},\ z_0 = \frac{\pi w_0^2}{\lambda} \quad (3.1)$$

w_0 is the input beam radius, $w(z)$ describes the radius of the beam along the propagation distance z, E_0 is the input beam field, z_0 is the Rayleigh range, λ is the wavelength, $r = r(x,y)$. Choosing the parameters $w_0 = 1$, $E_0 = 1$, and considering only one field component E_x, one obtains formula:

$$E_x(x,z) = \frac{1}{\sqrt{1+\frac{z^2\lambda^2}{\pi^2}}} \exp\left(\frac{-x^2}{1+\frac{z^2\lambda^2}{\pi^2}}\right) \tag{3.2}$$

The input fields distributions obtained with formula 3.2 and calculated in the program are shown on the figure 3.1.

For all of the performed simulations following parameters was used:

- number of points in the transverse (*x* and *y*) directions $N = M = 401$,
- calculation window width 40 x 40 μm
- single step length in the *x* and *y* directions $\Delta x = \Delta y = 0.1$ μm
- single step length in the z direction $\Delta z = 0.1$ μm
- propagation medium refractive index $n = 1$

The input field is presented on the figure 3.1. Example results are presented in figures 3.2 to 3.5.

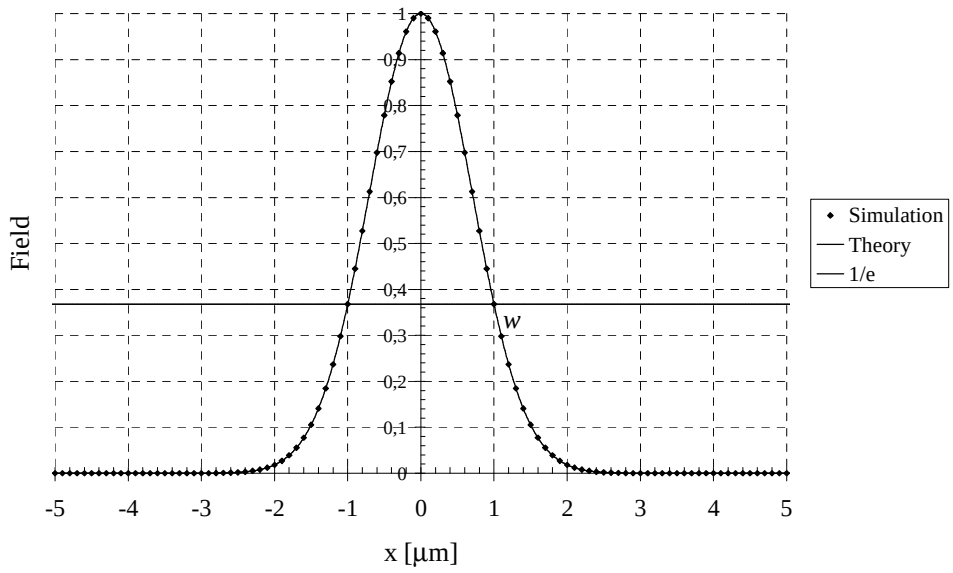

Figure 3.1. The input Gaussian beam profile with w = 1.

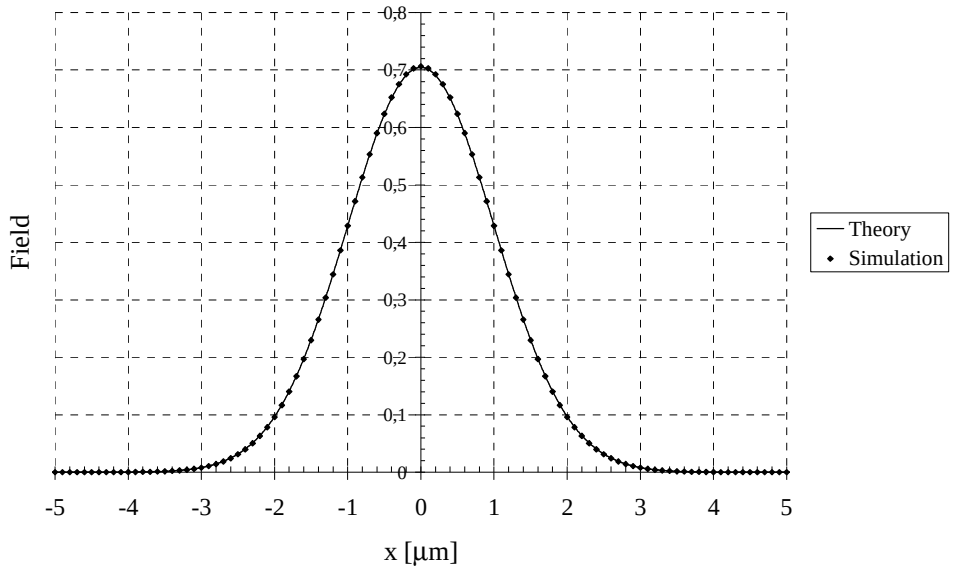

Figure 3.2. Comparison of the analytical result and simulation. Beam after propagation to 5 μm in free space, wavelength 632.8 nm.

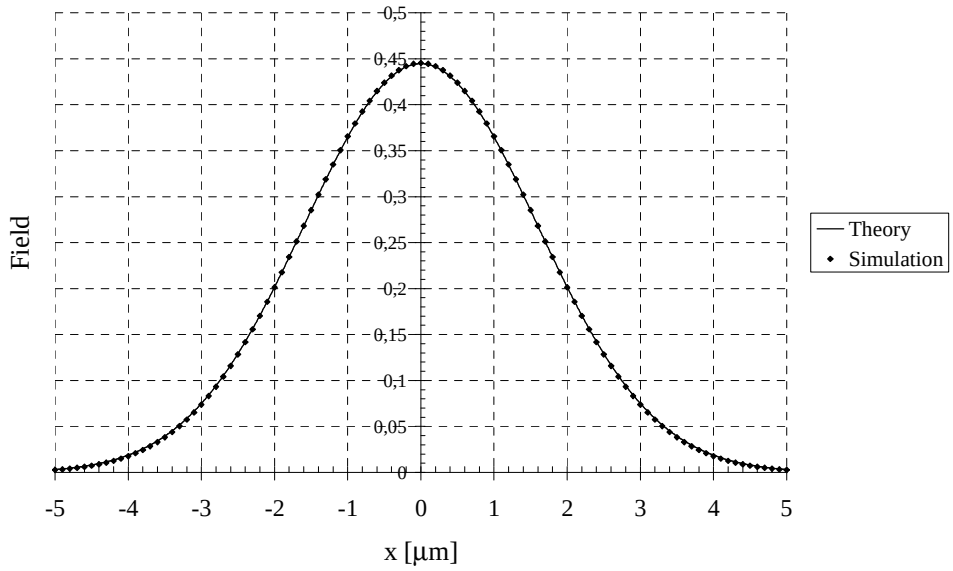

Figure 3.3. Comparison of the analytical result and simulation. Beam after propagation to 10 μm in free space, wavelength 632.8 nm.

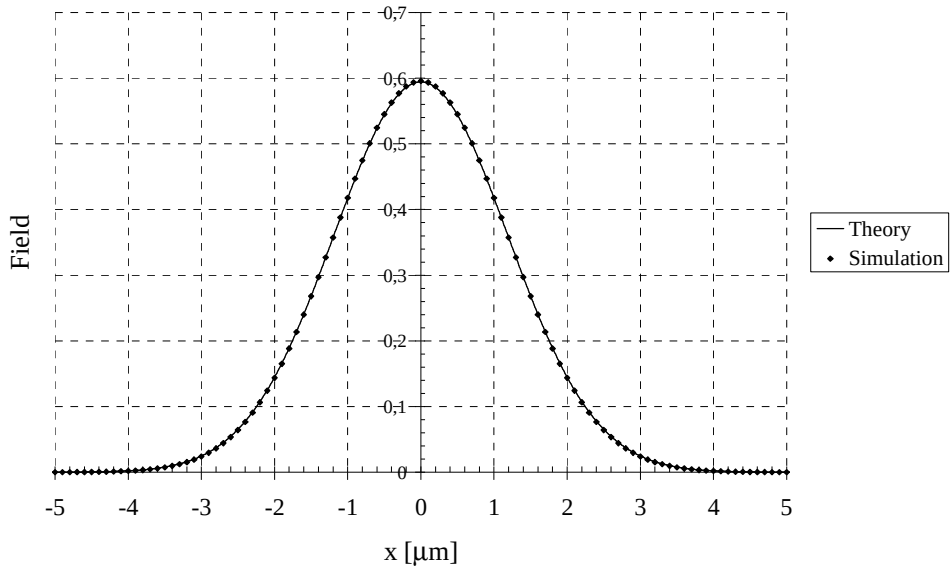

Figure 3.4. Comparison of the analytical result and simulation. Beam after propagation to 5 μm in free space, wavelength 850 nm.

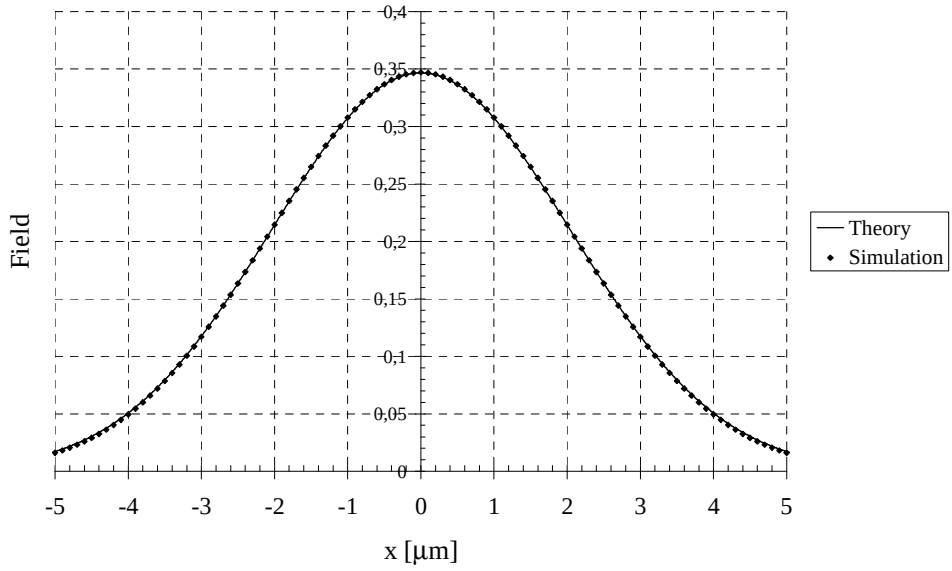

Figure 3.5. Comparison of the analytical result and simulation. Beam after propagation to 10 μm in free space, wavelength 850 nm.

Figures 3.2 to 3.5 show that the code calculates the field propagation in the free space with high accuracy for different parameters of the input field.

The computations was repeated for one of the cases with changed value of the propagation step *dz*, changed mesh density *dx*, *dy*, and with changed value

of the parameter α, to check the stability and accuracy of the code in dependence from this parameters.

Changes in the propagation step length *dz* are affecting the accuracy of the calculations. However the influence of change in the propagation step length in the range to 0.5 μm does not causes significant changes in the accuracy of the calculations. The values of the propagation step above 0.5 μm causes the degradation of the obtained calculation results. Figure 3.6 presents results of performed calculations for three different values of the propagation step length *dz*.

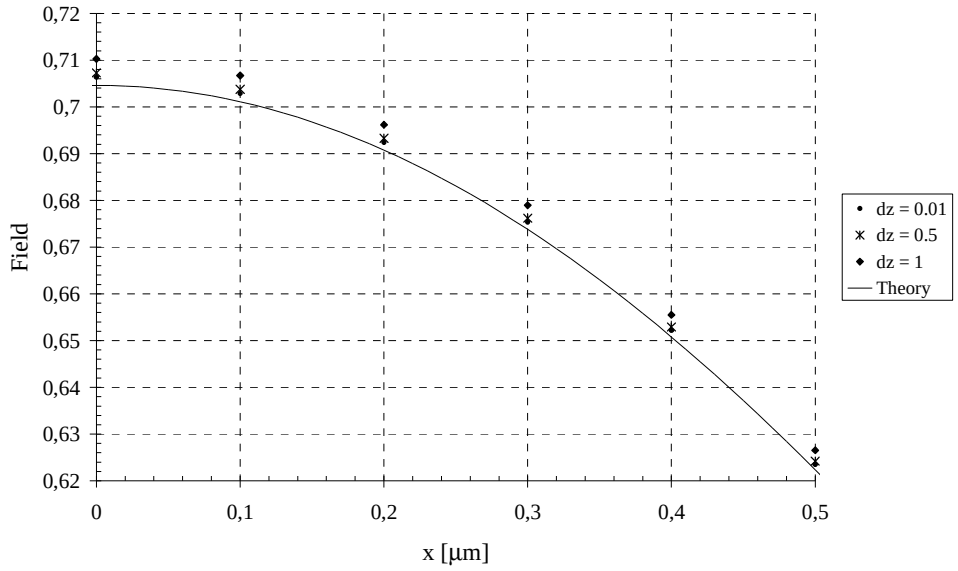

Figure 3.6. The comparison of the obtained calculation points for three different propagation step lengths.

The difference between calculations results are relatively small for the step lengths 0.5 and 0.1 in comparison with the simulation performed for the step length $dz = 1$. Figure 3.7 presents the results of the calculations for the propagation step $dz = 0.1$ and $dz = 0.01$, and it can be observed that making propagation step smaller does not bring any improvement in the accuracy of

the calculations. Because smaller value of the step length makes the calculations time much longer and does not improve the accuracy, it is not justified to make the propagation step smaller than 0.1 μm.

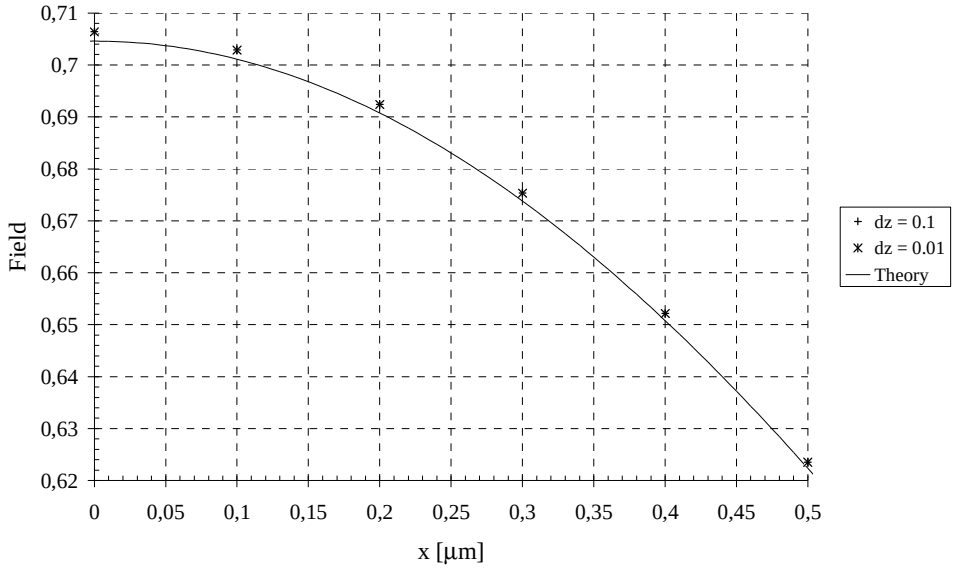

Figure 3.7. The difference between calculations results for the propagation steps dz = 0.1 and dz = 0.01.

Figure 3.8 is showing the accuracy of performed calculations for different values of the step size. The accuracy is described as the mean quadratic deviation (MQD) of the points calculated by program with respect to the results of the analytic calculations, according to formula:

$$MQD = \sqrt{\frac{\sum_{i=1}^{N}\left[E_T(i) - E_C(i)\right]^2}{\sum_{i=1}^{N}\left[E_T(i)\right]^2}} \tag{3.3}$$

where E_T are the points obtained with analytical calculations, E_C are the numerical results, N is the number of points along the x-axis.

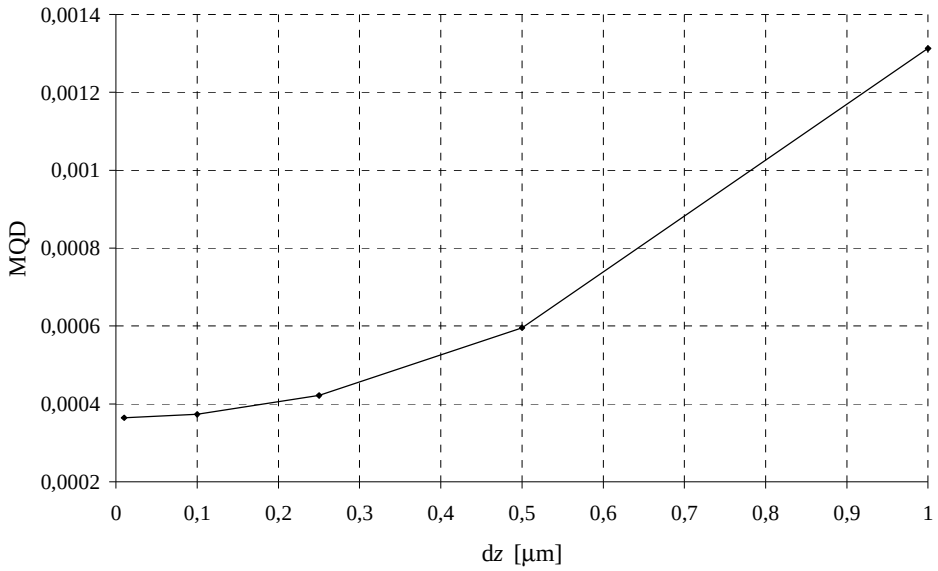

Figure 3.8. Mean Quadratic Deviation of the numerical result relative to the analytical result with respect to the propagation step length.

The beam profiles obtained analytically and with simulation for the step lengths 0.01 and 0.1 μm are very similar, with the MQD value less than $0.4 \cdot 10^{-3}$. Making the step length longer gives in result less accurate calculations.

Next, the accuracy of the numerical calculations was checked against changes in the mesh density. Presented program uses the rectangular, regular mesh of points where $dx = dy$. Figure 3.9 presents the theoretical line and points calculated for three different values of the mesh size.

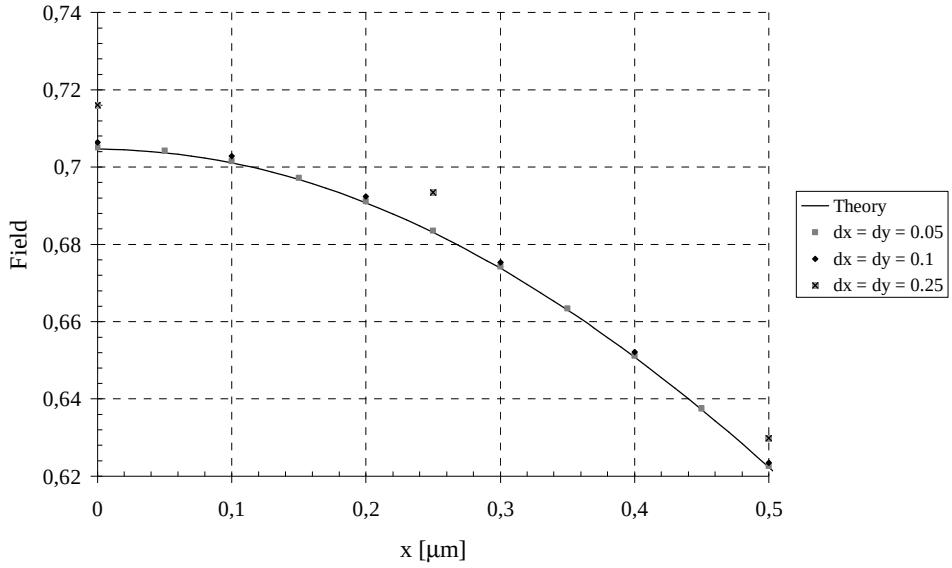

Figure 3.9. Numerical results obtained for three different values of the mesh size dx and dy [μm].

It can be observed, that the most accurate values are obtained for the smallest mesh size (in this case 0.05 μm). Figure 3.10 presents the mean quadratic deviation (MQD) calculated with formula 3.3 of results obtained with numerical simulation for different mesh sizes.

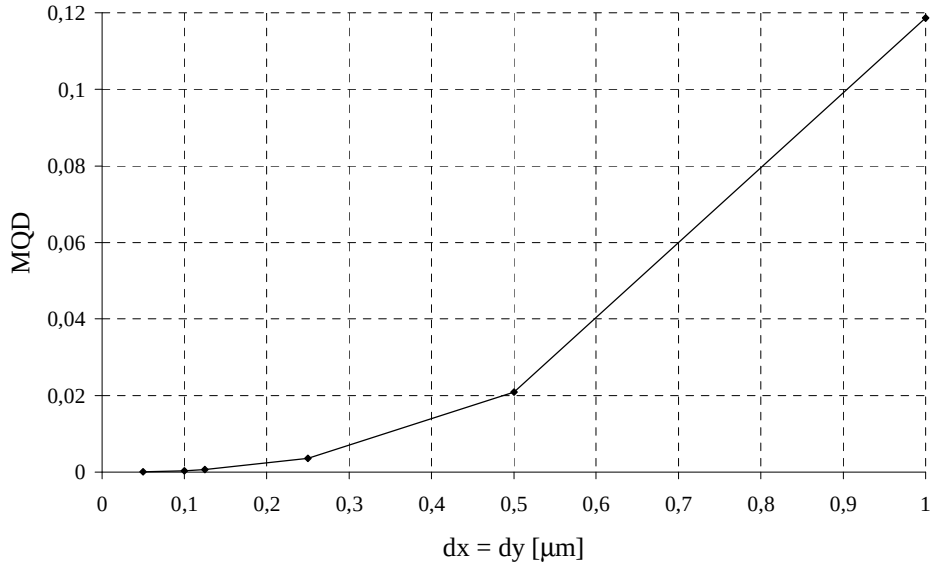

Figure 3.10. Mean Quadratic Deviation of the numerical result relative to the analytical result with respect to the mesh size (dx, dy).

The best results of performed calculations was obtained for the mesh size $dx = dy = 0.05$ [μm]. MQD calculated for this case has the value $7.08 \cdot 10^{-5}$ which means that the calculated values for this mesh are closest to the theoretical line – it can be observed on the figure 3.9. However calculations for this dense mesh consume much more memory and time. The value of the MQD obtained for the mesh with $dx = dy = 0.1$ [μm] is $0.4 \cdot 10^{-3}$, but the calculation time and computational cost of the simulation is very low comparing to the previous case. Using high density meshes for the calculations is justified only in case, when very high accuracy is needed, for example calculations in the PCF with complex structure of the cladding. Comparing figures 3.8 and 3.10 one can also observe; that changing the mesh density affects the calculation results more than changing the propagation step length. The code is much more sensitive for the changes in the density of the mesh used for calculation.

Parameter α responsible for the calculation scheme (implicit-explicit) does not affect the calculation results in the range from 0.5 to 1. Values of the parameter below 0.5 give unstable results, making the parameter α greater than 0.5 gives stronger effect of numerical dissipation – decreasing of the propagating signal power due to numerical effects.

Figure 3.11 presents the results of calculations for three different values of α parameter. It can be observed; that the points calculated with the program has a stable value in dependence with α. This parameter decides about the stability of the code, and does not affect the results of the calculations significantly. In further calculations the Crank-Nicholson scheme will be used, for which parameter $\alpha = 0.5$.

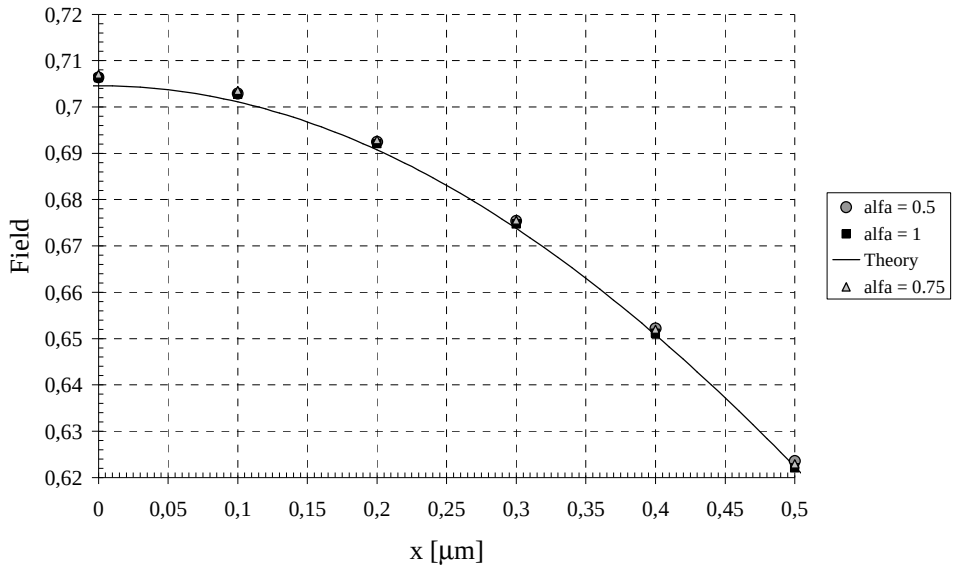

3.11. Numerical results obtained for three different values of the α parameter.

Developed code can be used to simulate the beam propagation inside the nonlinear medium. Due to check the accuracy of the nonlinear effect the Kerr-lens theorem for non-linear propagation was used. For a Gaussian beam with power P and beam radius w propagating through a thin layer (thickness d) of nonlinear medium with nonlinear index n_{NL}, the inverse focal length f^{-1} of the Kerr lens can defined as [19]:

$$f^{-1} = \frac{4n_{NL}d}{\pi w^4} P \tag{3.4}$$

The Kerr-lens focal length was calculated analytically with use of the formula (3.4), and also by measuring of the beam width after propagation to 2 μm. With known input Gaussian beam width w, and known width of the beam w_1 after propagation on a distance d, the Kerr-lens focal length can be estimated with formula:

$$f = \frac{wd}{\Delta w} \tag{3.5}$$

where $\Delta w = w - w_1$.

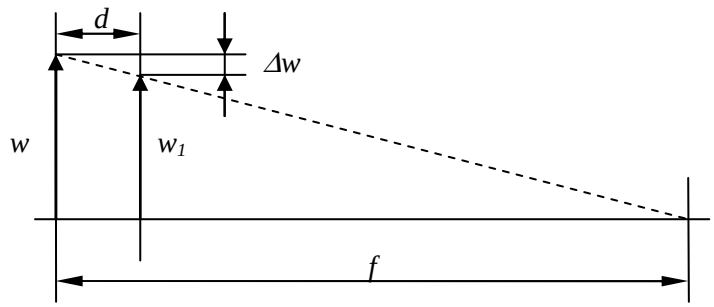

Figure 3.11. Geometrical construct used for estimation of the Kerr lens focal length.

Formula 3.5 is the estimation from the geometric construction shown in figure 3.11. Results obtained for two different wavelengths are presented in figures 3.12 to 3.14.

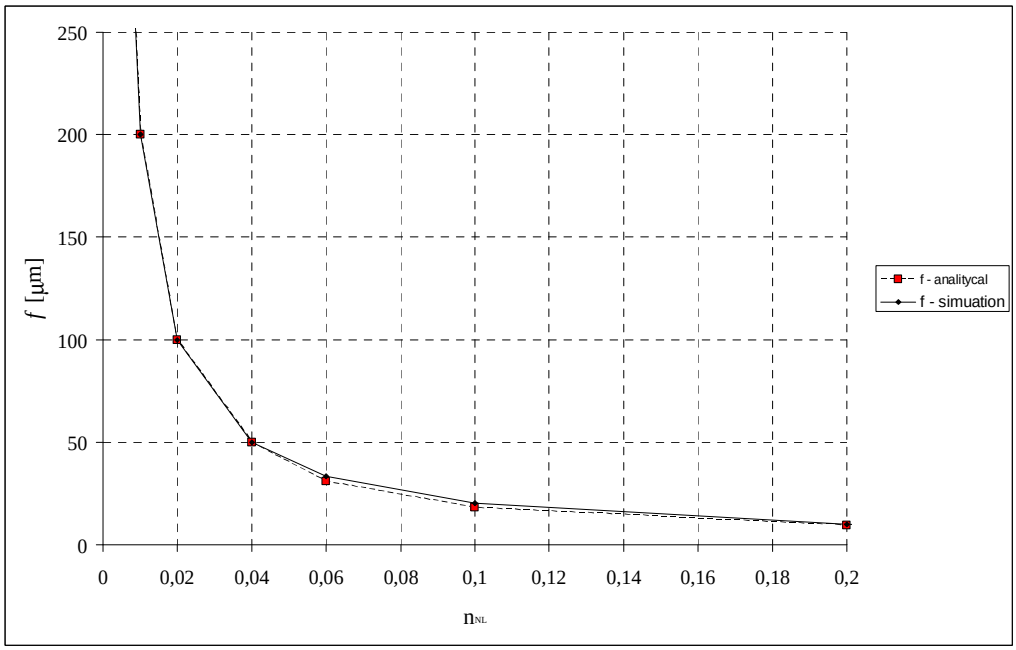

Figure 3.12. Estimated with formula 3.5 and calculated with formula 3.4 values of Kerr lens focal lengths. Wavelength 638.2 nm.

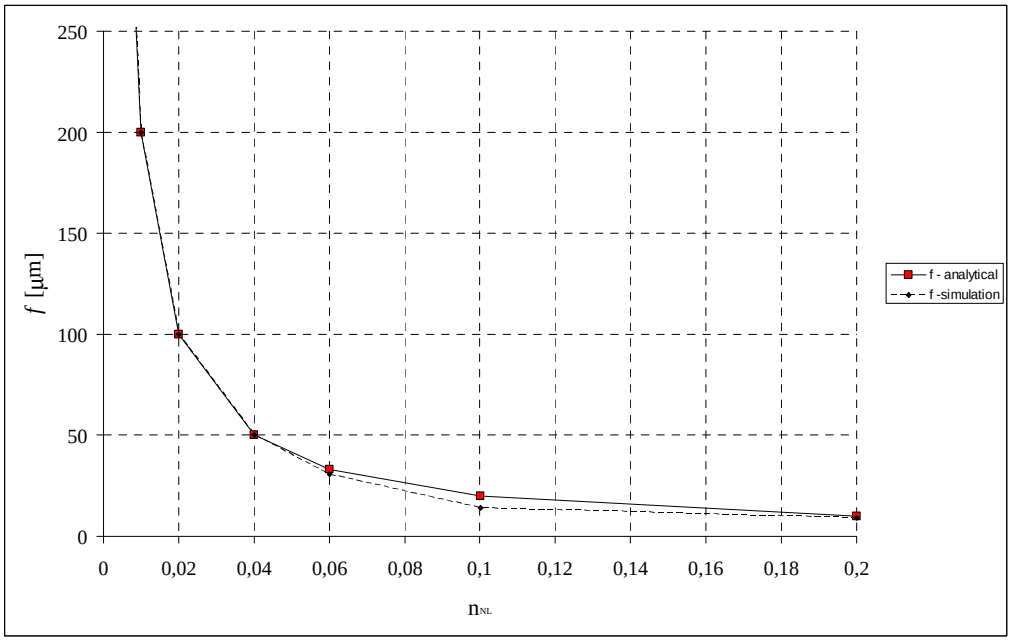

Figure 3.13. Estimated with formula 3.5 and calculated with formula 3.4 values of Kerr lens focal lengths. Wavelength 850 nm.

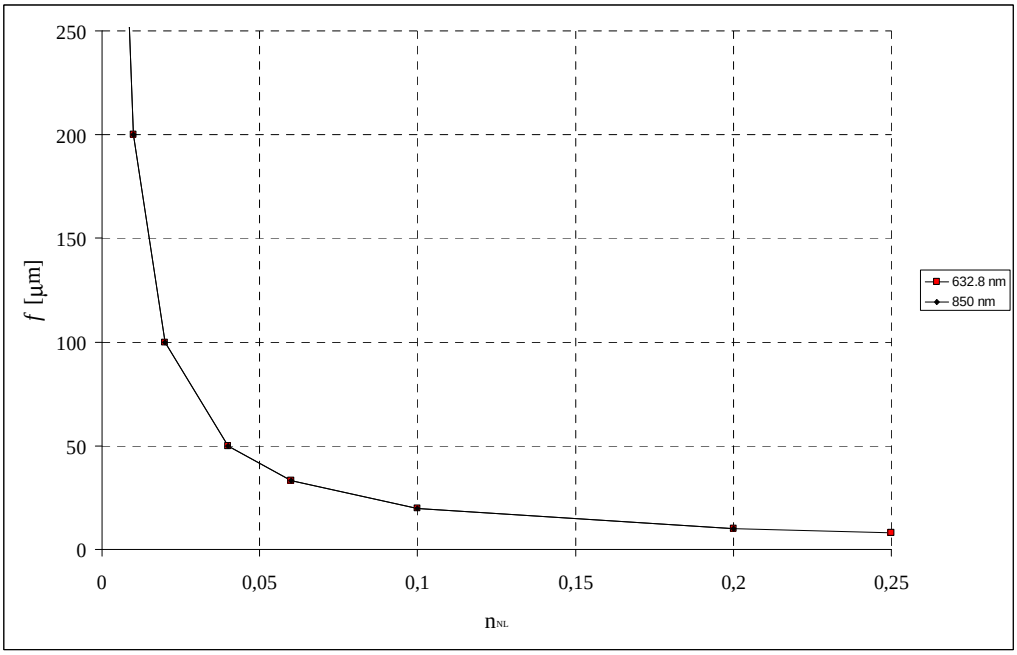

Figure 3.14. Comparison between the Kerr lens focal length obtained for two different wavelengths.

The agreement between results obtained with the theory of the Kerr lens focal length and the simulation with FD-BPM program shows that the nonlinearity implemented in the code works well. This test may be not very demanding, due

to low differences in the beam width Δw after propagation for a small distance, especially in the medium with low nonlinearity, but the nonlinear effect implemented in the presented program acts exactly the same like in theoretic model of the Kerr lens. Formula 3.4 is wavelength independent, thus different wavelength of the beam should not affect the nonlinear self-focusing. The shape of the curve and the values of the obtained focal lengths presented on the figure 3.14 shows, that for two different wavelengths this value stays almost the same.

4. Propagation inside the fibre.

Validation of the developed code presented in section 3 was performed for the free space propagation of the Gaussian beam. Obtained results are consistent with the theory, the program works well for the propagation in a free space, which is homogenous – without additional defects. The optical fibre is a waveguide – a structure built of at least two different materials, with different parameters. Especially a PCF is a complicated structure in which the cladding area is a photonic crystal built of two or more materials (most often glass + air). Program needs validation in case of simulations for more complex structures. Accurate analytical solution of the field distribution inside PCF is impossible to obtain. Thus at first the program will be checked in case of propagation inside of the step index fibre (single-, and multi-mode). Calculations made with the developed program will be compared against some examples and theoretical results.

The step index fibre is a cylindrical waveguide propagating light inside the dielectric core area with the refraction index n_1, surrounded by

the dielectric core area with the refraction index n_2. The condition for guiding the light inside the core of the fibre is $n_1 > n_2$. The simplest explanation for the guiding phenomena is the Total Internal Reflection (TIR) on the boundary surface between the core and the cladding. Each fibre is characterized with the normalized frequency V, which gives the information about the number of modes allowed in the fibre for a given wavelength λ. This value is defined with formula:

$$V = \frac{2\pi a}{\lambda}\sqrt{n_1^2 - n_2^2} \tag{4.1}$$

where a is the core radius, λ is the wavelength of the propagating field, n_1 is the refractive index of the fibre core, and n_2 is the refractive index of the cladding. Single mode fibre characterizes with the normalized frequency V value less than 2.4 [16].

4.1. Real-Distance Mode Solving.

Real-Distance Mode Solving (R-DMS) technique allows for calculation of the propagation constant (β) value for every mode of the simulated waveguide [19]. The solution of the wave equation can be formally written as:

$$\mathbf{\Psi_t}(x,y,z) = e^{-jz\mathbf{H}}\mathbf{\Psi_t}(x,y,0) \tag{4.1.1}$$

In the waveguide with uniform index distribution along the z direction, an arbitrary input field $\mathbf{\Psi_t}(x,y,0)$ can be represented by the linear combination of the eigenmodes $\mathbf{\Phi_m}(x,y)$ in the structure:

$$\mathbf{\Psi_t}(x,y,0) = \sum_{m=0}^{\infty} a_m \mathbf{\Phi_m}(x,y) \tag{4.1.2}$$

where the summation includes both the guided modes and the radiation modes. The eigenvalue $\Delta\beta_m$ and eigenvector $\mathbf{\Phi_m}(x,y)$ of $\mathbf{H}$ satisfy:

$$\mathbf{H\Phi_m}(x,y) = \Delta\beta_m \mathbf{\Phi_m}(x,y) \tag{4.1.3}$$

By applying Taylor expansion to $e^{-jz\mathbf{H}}$ and making use of (4.1.3), (4.1.2) can be written as:

$$\mathbf{\Psi_t}(x,y,z) = \sum_{m=0}^{\infty} a_m \exp(-j\Delta\beta_m z)\mathbf{\Phi_m}(x,y) \tag{4.1.4}$$

Introduce the correlation function:

$$P(z) = \iint \mathbf{\Psi_t}^H(x,y,0)\mathbf{\Psi_t}(x,y,z)dxdy \tag{4.1.5}$$

where the superscript "*H*" denotes the Hermitian transpose. Substituting (4.1.3) and (4.1.4) into (4.1.5) and using the mode orthogonality, (4.1.5) becomes

$$P(z) = \sum_{m=0}^{\infty} \iint a_m^* \mathbf{\Phi}_\mathbf{m}^H(x,y) a_m \exp(-j\Delta\beta_m z) a_m \mathbf{\Phi_m}(x,y)\,dxdy = \sum_{m=0}^{\infty} A_m \exp(-j\Delta\beta_m z) \tag{4.1.6}$$

where $A_m = |a_m|^2 \iint \mathbf{\Phi}_\mathbf{m}^H(x,y)\mathbf{\Phi_m}(x,y)\,dxdy$.

That is a vector which consists of two components in full-vector case. Although (4.1.6) is derived from the full vector formula, it is easily to reduce the formula to the semi-vector case by using the major component in (4.1.6). The Fourier transform (FT) of (4.1.6) leads to an expression:

$$\tilde{P}(\Delta\beta) = \sum_{m=0}^{\infty} A_m \delta(\Delta\beta - \Delta\beta_m) \tag{4.1.7}$$

which suggests that the calculated spectrum will display a series of sharp resonant peaks, which correspond to the eigenmodes of the waveguide. The main advantage of the FT method is that the sharp resonant peaks of

the spectrum make it very easy to distinguish the modes even when the propagation constants between the modes are close to each other. However this method requires simulation for a long distance, with use of the small *dz* step. Choosing the step size too long will cause the resolution of the FT calculations to be too small, and the resonant peaks localized closer than the resolution won't be visible. This method is very accurate, and allows calculating the propagation constants β for all modes with one simulation, but requires big numerical effort.

4.2. Propagation in a step-index fibre.

The code has to be verified with some known example results. The R-DMS scheme allows for the estimation of the propagation constants values of the fibre modes. This algorithm can be checked by comparing the results obtained with calculations to some known and well described structure, or with results obtained with use of another numerical tool. The fibres described in [20] are multi- and single-mode. The mode propagation constants were calculated with use of commercial software FEMLAB. FEMLAB is an interactive environment for modelling and solving scientific and engineering problems based on partial differential equations (PDE's). When solving the PDE that describe a model, FEMLAB applies the finite element method (FEM). FEMLAB runs that method in conjunction with adaptive meshing and error control, thus it can be treated like an independent source of the accurate result. Reference [20] contains detailed analysis of the optical fibre with the core radius $a = 2$ μm, core refractive index $n_1 = 1.452$, cladding refractive index $n_2 = 1.43748$, wavelength of the propagating field

λ = 632.8 nm. The values of the modes propagation constants β and effective refractive indices n_{eff} are placed in table 4.2.1.

Table 4.2.1. Propagation constants of the fibre under investigation calculated with FEMSIM.

Mode number	β	n_{eff}
1	1,44073E+07	1,45101
2	1,43922E+07	1,44949
3	1,43723E+07	1,44748
4	1,43655E+07	1,44680
5	1,43482E+07	1,44505
6	1,43349E+07	1,44371
7	1,43202E+07	1,44223
8	1,43005E+07	1,44025
9	1,42950E+07	1,43970
10	1,42886E+07	1,43905

To check the accuracy of the applied method the same values should be obtained with the simulation with use of the code presented in this work.

Values used in the performed simulation:

- number of points in the transverse (x and y) directions $N = M = 401$,
- calculation window width 40 x 40 μm
- single step length in the x and y directions $\Delta x = \Delta y = 0.1$ μm
- single step length in the z direction $\Delta z = 0.01$ μm
- number of steps $N = 200000$ (propagation length – 2 mm)
- fibre core refractive index $n_1 = 1.452$
- fibre cladding refractive index $n_2 = 1.43748$

The calculations were performed with use of the computational server available at the National Institute of Telecommunications in Warsaw. Although this server is a powerful machine (dual core 2.41 GHz processor, 3.75 GB RAM memory), the calculation for the parameters listed above takes about three days. The fibre was excited with the Gaussian beam off the axis of the structure, to excite all the fibre modes. The field in the fibre after propagation length z = 2 mm is shown in figure 4.2.1.

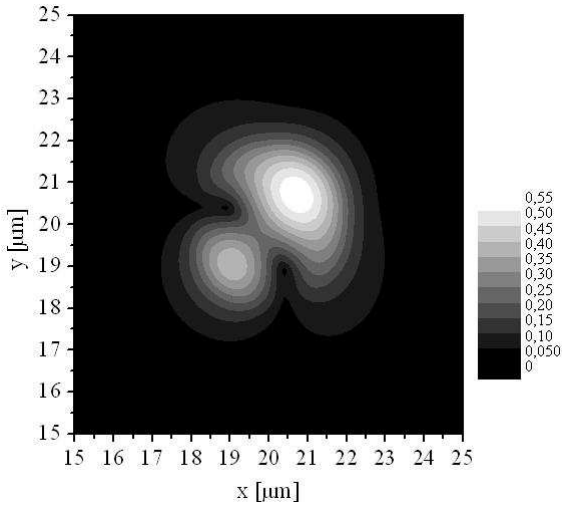

Figure 4.2.1. The field inside the simulated fibre after propagation to 2 mm.

It can be observed, that the field is oscillating inside the fibre, it is the superposition of the excited modes. Very short propagation step size *dz*, and relatively long distance of the propagation, should give enough resolution of the Fast Fourier Transform (FFT) to recognize and separate all resonant peaks. In the table 4.2.1 can be found values of the propagation constants and the effective indices for ten modes of the investigated fibre. Due to finished number of modes in this fibre, the values of the β and n_{eff} parameters are expected to be found in the range (1.43748, 1.452). The starting value of the effective index was set to $n_{eff0} = 1.438$, and didn't change during propagation. That means that the values of the Δn_{eff} are expected to be from

the range 0 to 0.014. Figure 4.2.2 shows the FFT amplitude corresponding to the values of Δn_{eff} in this range.

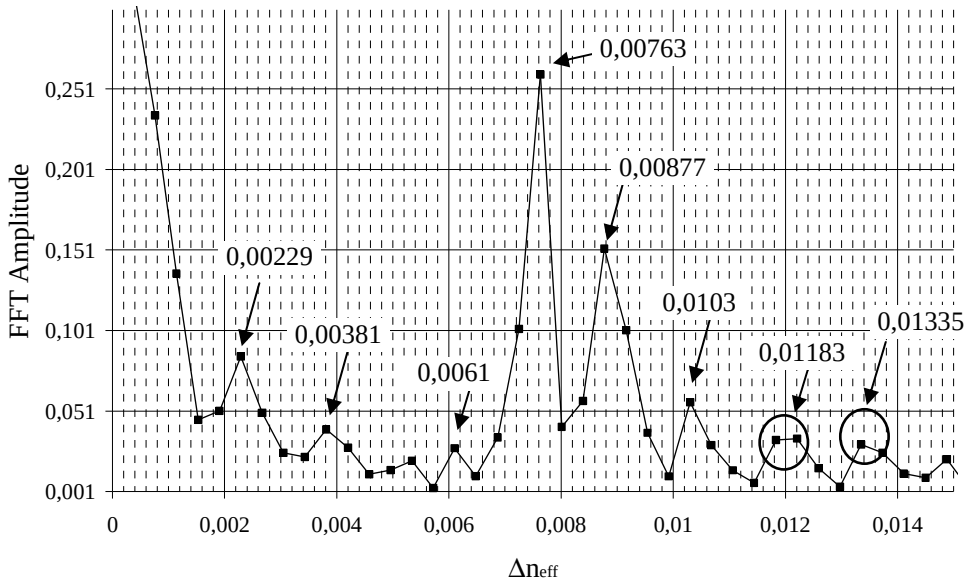

Figure 4.2.2. The series of resonant peaks corresponding to the values of the modes effective refractive indices.

On the figure 4.2.2 six different peaks can be localized, but it can be observed, that resolution obtained with this simulation can be not enough to observe the values corresponding to all modes. With support of known and expected results, two more peaks were considered as the Δn_{eff} values obtained in performed simulation (marked in Fig. 4.2.2 with circles). Moreover, the amplitude of some peaks obtained is relatively small, and the noise of performed FFT can affect the results. The values read of the performed FFT are enclosed in the table 4.2.2.

Table 4.2.2. Comparison of n_{eff} values.

Δn_{eff}	n_{eff}	FEMSIM	$\Delta\varepsilon$	Mode number
0,00229	1,44029	1,44025	4E-05	8
0,00381	1,44181	1,44223	0,00042	7
0,0061	1,4441	1,44371	0,00039	6
0,00763	1,44563	1,44505	0,00058	5
0,00877	1,44677	1,4468	3E-05	4
0,0103	1,4483	1,44748	0,00082	3
0,01183	1,44983	1,44949	0,00034	2
0,01335	1,45135	1,45101	0,00034	1

$\Delta\varepsilon$ is the difference between the values obtained with R-DMS simulation and the values obtained with FEMSIM. These values may not differ much from each other, but important thing is, that the mode effective indices values of different modes are also very close. Above example was repeated with a ten times smaller value of the propagation step size. The number of propagation steps has not changed. The obtained FFT for the same range of Δn_{eff} as in before simulation is shown in figure 4.2.3. The field inside the fibre is presented in figure 4.2.4.

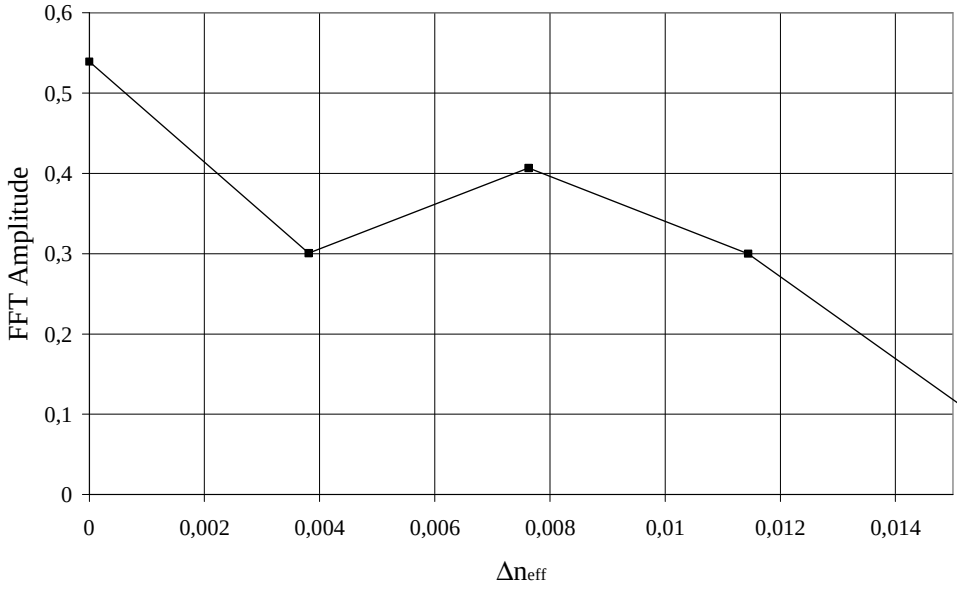

Figure 4.2.3. Results obtained with the step size dz = 0.001; 200.000 steps, propagation length 200 μm.

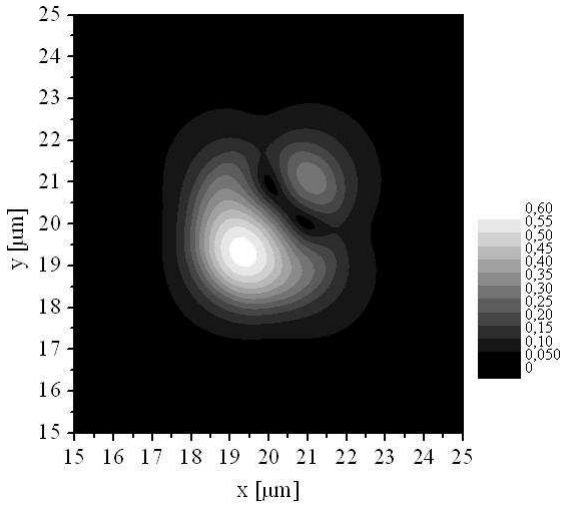

Figure 4.2.4. The field inside the simulated fibre after propagation to 200 μm.

The results presented in the figure 4.2.3 do not bring any information about the fibre modes. The propagation length is too short to obtain resonant peaks in the considered range of the Δn_{eff}. The step size may be shorter, but the information carried by the correlation function (4.1.5) is not good enough. Obtaining better results means the simulation for at least the same propagation length with the step size like in the second simulation. The single step

calculation time did not change, which means, that it is impossible to repeat the simulation for the same range – 2 mm. Such simulation would need 2.000.000 steps of calculations, which gives approximately 25 days of single program run. The R-D method requires relatively long distance of the propagation length with very short single step of propagation. Application of this method in the code developed at the National Institute of Telecommunications is extremely ineffective.

4.3. Propagation in Photonic Crystal Fibre.

The PCF was described in Section 1.2. It is a structure with the cladding built of Photonic Crystal (PC). This PC is characterized with some mean value of the refractive index (see Fig. 1.2.7 a), and due to that it can be assumed that a solid core PCF has an equivalent step-index fibre, with similar characteristics. Due to that, the code validated in case of the propagation inside a step-index fibre should work well in case of the propagation inside the solid core PCF. However, the level of complication of the photonic crystal, as a periodic structure with many elements, is much higher than simple step-index fibre, thus the discretization of the PCF structure for the calculations should be more accurate.

The main task in this work was to adapt the code and validate it for the propagation the PCF's. Analysis performed in Section 4.2 brings first concerns about the ability of the developed code to operate accurately in case of the propagation inside the PCF. The most important issue is the time of the calculations, which increases significantly for the calculations with use of a dense mesh of points.

First simulations were performed for the structure shown in figure 4.3.1, for the set of the parameters:

- pitch $\Lambda = 2$ mm
- hole diameter $d = 0.8$ mm
- material refractive index $n_1 = 1.46$
- hole refractive index $n_2 = 1$
- propagating wavelength $\lambda = 632$ nm

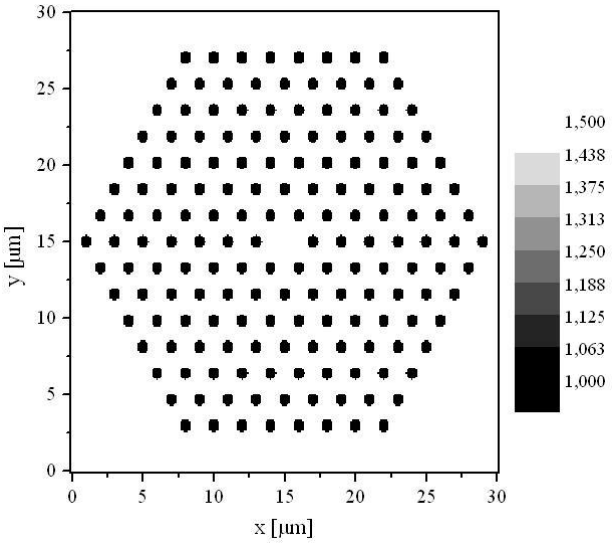

Figure 4.3.1. The cross-section of the simulated structure.

The parameters of the simulation:

- number of points in the transverse (x and y) directions $N = M = 301$,
- calculation window width 30 x 30 μm
- single step length in the x and y directions $\Delta x = \Delta y = 0.1$ μm
- single step length in the z direction $\Delta z = 0.1$ μm
- effective refractive index $n_{eff} = 1.46$.

The evolution of the propagating field is shown in figure 4.3.2. The simulated fibre maintains the field inside the core; the light is propagating in the structure with no additional effects.

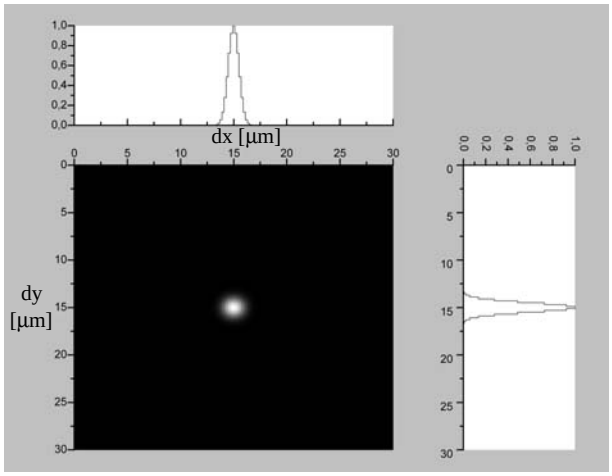

(a) Input field at z = 0

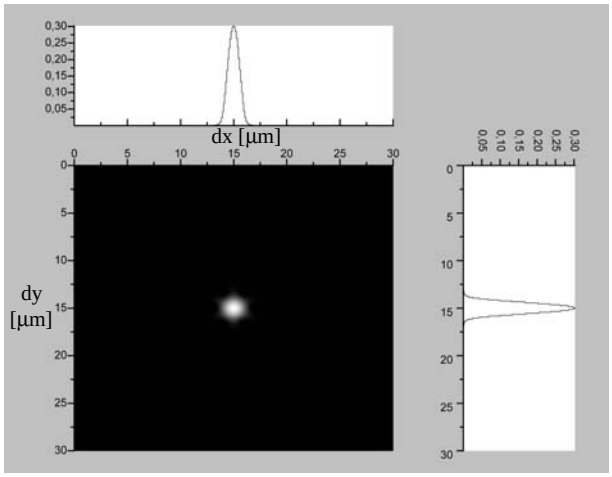

(a) The field distribution at z = 2 mm

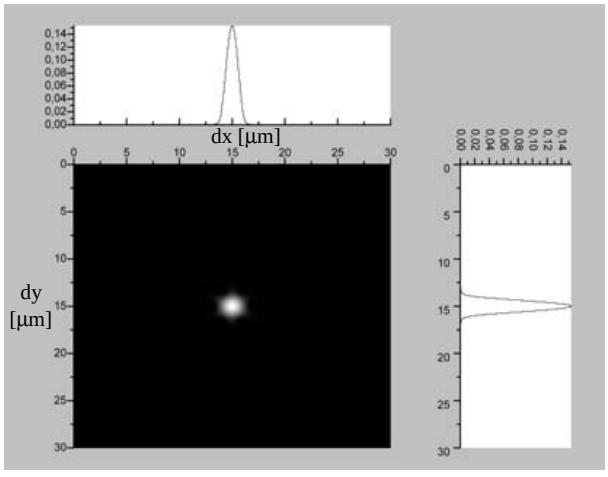

(a) The field distribution at z = 6 mm

Figure 4.3.2. Calculations for the propagation inside the PCF.

The program seems to work well in case of the calculations presented above. However further analysis of the code brings some fault results. Presented

program was created for the assumption of the paraxial propagation. This assumption makes the calculations easier to perform, but the simulation in the fibre with a larger core area gives unstable solutions. Figure 4.3.3 shows the field distribution inside the PCF large area core. Some bright spots of the light intensity can be observed at the boundary surface between the material and the air hole. The energy of the propagating field is growing (presented in figure 4.3.4), the code becomes unstable.

The parameters used for the simulation:

- number of points in x and y direction $N = M = 501$,
- calculation window width 25 x 25 μm
- single step length in the x and y direction $\Delta x = \Delta y = 0.05$ μm
- single step length in the z direction $\Delta z = 0.05$ μm
- propagation medium refractive index $n_1 = 1.45$
- air hole refractive index $n_2 = 1$
- wavelength $\lambda = 1$ μm

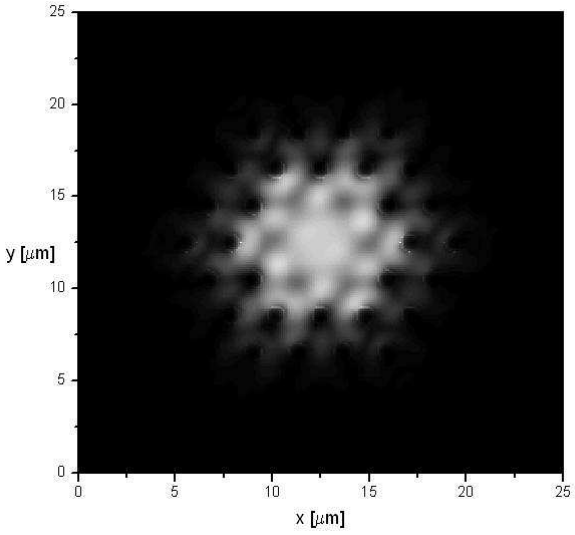

Figure 4.3.3. Instability of the code observed at the boundary surface between the material and the air hole in case of the propagation in the PCF fibre with large core area (7 holes missing).

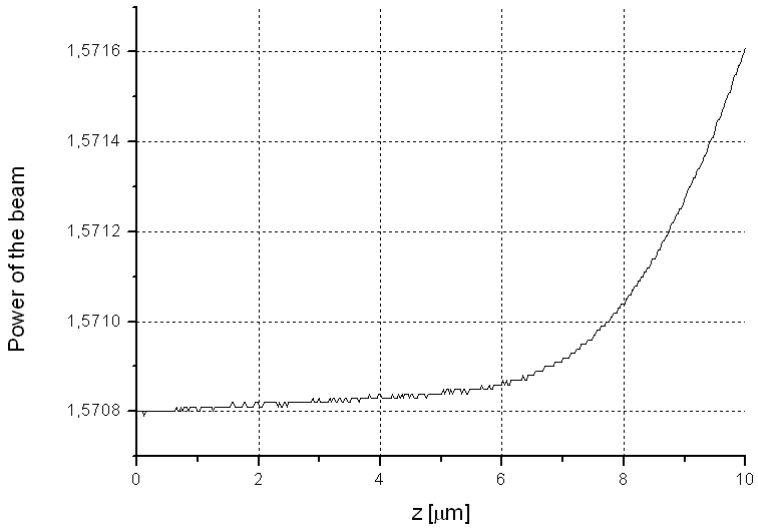

Figure 4.3.4. Instability of the beam power during propagation.

This kind of the power increase at the boundary surface occurs also for the large area of the air filled hole inside the fibre. After propagation for a certain length z, the field infiltrates the air hole area, and becomes very unstable. The example propagation process is shown in figure 4.3.5, the parameters used for the simulation are close to values used in previous simulation, however the air hole is now much bigger.

The parameters used for the simulation:

- number of points in x and y direction $N = M = 401$,
- calculation window width 20 x 20 μm
- single step length in the x and y direction $\Delta x = \Delta y = 0.05$ μm
- single step length in the z direction $\Delta z = 0.1$ μm
- propagation medium refractive index $n_1 = 1.45$
- air hole refractive index $n_2 = 1$
- wavelength $\lambda = 1$ μm

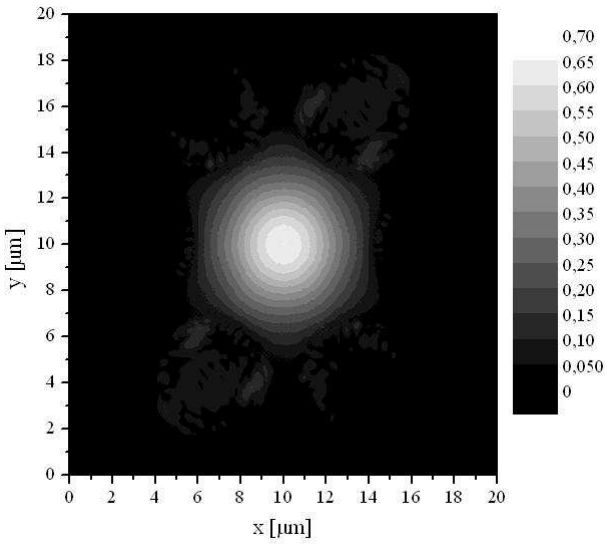

Figure 4.3.5. The propagation inside the structure with one ring of holes.

This effect disqualifies the developed code as the numerical tool for the analysis of the PCF's of different types. The instability of the code presented above could be explained with the high index contrast at the boundary surface between the propagation medium and the air filled hole, but it cannot be the only effect, due to simulations performed for the fibre presented in figure 4.3.1, which were stable. The index contrast in all presented cases was nearly the same, but two last examples gives unstable results. It can be observed, that the core area of the last two simulated structures is much bigger than the first one. The code is built with assumption of the paraxial propagation – this may lead to the conclusion, that this algorithm can be used only for a precise set of the structure parameters (large cladding area filled with relatively small air holes, fibre core in only one defect of the simulated structure). The code could be changed to include some additional effects, and improve its abilities. However present time of the single step calculations, which depends on the complication level of the structure and has a value from several to a dozens of seconds, is extremely long. The example simulation of

the fibre of 1 m length with the parameters $\Delta z = \Delta x = \Delta y = 0.1$ μm would take approximately 115 days (for assumption of a single step calculation time equal 1 second). The calculation time of presented algorithm makes it impractical in providing research and modelling of the PCF's. The narrow specification of the simulated structure is also a big problem.

5. Conclusions.

The main goal for this work was to adapt the software developed at the National Institute of Telecommunications for the simulations of different types of the Photonic Crystal Fibres (PCFs). The code was written with use of FORTRAN programming language, and allows for the simulation of the light propagation in linear and nonlinear mediums. The program was validated and upgraded during the project realization. Some functions were added to improve the accuracy of the calculations and its stability. This change in the code has also brought about an unwanted extension effect on the calculation time, which was already extremely long.

Section 3 of this dissertation describes the process of the developed code validation in the case of free space propagation. The homogenous structure allows for very stable and accurate simulation of the beam. The Transparent Boundary Conditions (TBC) used allows for the signal to radiate outside the calculation window, not affecting the propagating beam. The nonlinear effect was added to the calculations and its accuracy was checked in section 3. The code is working well in case of the propagation in free space.

The Real-Distance Mode Solving Technique described in section 4.1 allows for calculations of the effective indices of the fibre modes, but the application of

this method in presented algorithm turned out to be technically difficult due to the extremely long time of the calculations needed to obtain results with sufficient accuracy.

More complicated structures, like PCF's, simulated with use of presented algorithm needs to be described with an adequately dense mesh, in order to minimize the staircasing effect. This requirement makes simulations in PCF's even more time consuming. Moreover, the presented algorithm is found to be stable only for one type of PCF structure, making the core and the hole area larger generates instability of the calculation, as presented in section 4.3.

It is concluded that, due to the extremely long time of the calculations, and stability problems in some PCF structures, the algorithm described cannot be considered as an accurate numerical tool for the simulation of the photonic structures. A suggested alternative for the numerical simulation of waveguides of arbitrary cross-section such as PCFs is to use a non-uniform rectangular grid, as suggested by Hadley in [21].

References:

[1] Lord J. W. S. Rayleigh: On the maintenance of vibrations by forces of double frequency, and on the propagation of waves through a medium endowed with a periodic structure, *Philosophical Magazine*, vol. 24, pp. 145–159, 1887

[2] E. Yablonovitch: Photonic Band-Gap Structures, *J. Opt. Soc. Am. B*, vol. 10, no. 2, pp. 283-295, February 1993

[3] S. G. Johnson, J. D. Joannopoulos: Introduction to Photonic Crystals: Bloch's Theorem, Band Diagrams, and Gaps (But No Defects) [online], available at: <URL: http://ab-initio.mit.edu/photons/tutorial/photonic-intro.pdf>
[Accessed 2 October 2007]

[4] P. Russell: Photonic Crystal Fibres, *Science*, vol. 299, pp. 358-362, 2003

[5] G.Humbert, J. C. Knight, G. Bouwmans, P. St. J. Russell: Hollow Core Photonic Crystal Fibres for Beam Delivery, *Optics Express*, vol. 12, no. 8, pp. 1477-1484, 2004

[6] J. C. Knight, T. A. Birks, P. St. J. Russell, D. M. Atkin: All-silica single-mode optical fiber with photonic crystal cladding, *Opt. Lett.*, vol. 21, pp. 1547-1549, 1996; Errata, *Opt. Lett.*, vol. 22, 484, 1997

[7] T. A. Birks, J.C. Knight, B.J. Mangan, P.St.J. Russell: Photonic crystal fibers: an endless variety, *IEICE Trans. Electron.*, vol. E84-C, pp. 585-592, 2001

[8] J. C. Knight, T. Birks, R. Cregan, P. Russell, J. Sandro: Large mode area photonic crystal fiber, *Electron. Lett.*, vol. 34, pp. 1347-1348, 1998

[9] B. J. Mangan, J. Arriaga, T. A. Birks, J. C. Knight, P. S. J. Russell: Fundamental-mode cutoff in a photonic crystal fiber with a depressed-index core, *Opt. Lett.*, vol. 26, pp. 1469-1471, 2001

[10] R. F. Cregan, B. J. Mangan, J. C. Knight, T. A. Birks, P. S. J. Russell, P. J. Roberts, D. C. Allan: Single-Mode Photonic Band Gap Guidance of Light in Air, *Science*, vol. 285, pp. 1537-1539, 1999

[11] F. Couny, F. Benabid, P. S. Light: Large Pitch Kagome-Structured Hollow-Core PCF, *Post deadline Paper Th4.2.4 at the Proceedings of the ECOC conference*, Cannes, France, 2006

[12] L. Adamowicz, Q. Van Nguyen: Electromagnetic field in a slab of photonic crystal by BPM, *Optics and Lasers in Engineering*, no. 35, pp. 67-78, 2001

[13] A. Ferrando, E. Silverstre, J. J.Miret, P. Andes and M. V. Andes: Full-vector analysis of a realistic photonic crystal fibre, *Opt. Lett.*, vol. 24, pp. 276-278, 1999

[14] F. Fogli, L. Saccomandi, P. Bassi: Full vectorial BPM modeling of Index-Guiding Photonic Crystal Fibres and Couplers. *Optics Express*, vol. 10, no. 1, pp. 54-59, 2002

[15] G. R. Hadley: Transparent Boundary Condition for the Beam Propagation Method, *Journal of Quantum electronics*, vol. 28, no. 1, pp. 363-370, 1992

[16] A. P. Agrawal: *Nonlinear Fiber Optics.* Academic Press, San Diego, 1995

[17] O.V. Sinkin, R. Holzlöhner, J. Zweck, and C. R. Menyuk: Optimization of the Split-Step Fourier Method in Modeling Optical Fibre Communications Systems, *Journal of Lightwave Technology*, vol. 21, no. 1, January 2003

[18] Kerr lens, RP Photonics, Encyclopedia of Laser Physics and Technology [online], available at:<URL: http://www.rp-photonics.com/kerr_lens.html>
[Accessed 26th March 2007].

[19] N.-N. Feng, G.-R. Zhou, W.-P. Huang: Mode calculation by Beam Propagation Method combined with digital signal processing technique, *Quantum Electronics*, vol. 39, no. 9, pp. 1111-1117, 2003

[20] T. Kozacki: Eletro-Magnetic Field Distribution in a Fibre [online]
available at:<URL: http://zto.mchtr.pw.edu.pl/download/100.pdf>
[Accessed 2nd February 2008]

[21] G. R. Hadley: Numerical Simulation of Waveguides of Arbitrary Cross-Section, *Int. J. Electron. Commun*., vol. 58, pp. 1-7, 2004